Artificial transneurons emulate neuronal activity in different areas of brain cortex

Rivu Midya[1,*], Ambarish S. Pawar[2,**], Debi Pattnaik[3], Eric Mooshagian[2,4], Pavel Borisov[3], Thomas D. Albright[2], Lawrence H. Snyder[5], R. Stanley Williams[6], J. Joshua Yang[1,7,#], Alexander G. Balanov[3,#], Sergei Gepshtein[2,8,#], Sergey E. Savel'ev[3,#]

[1] Department of Electrical and Computer Engineering, University of Massachusetts, Amherst, MA, 01003 USA
[2] Systems Neurobiology Laboratories, Salk Institute for Biological Studies, La Jolla, CA 92037, USA
[3] Department of Physics, Loughborough University, LE11 3TU, UK
[4] Department of Cognitive Science, University of California San Diego, La Jolla, CA 92093, USA
[5] Department of Neuroscience, Washington University School of Medicine, St. Louis, Missouri 63110, USA
[6] Department of Electrical and Computer Engineering, Texas A&M University, College Station, Texas 77843, USA
[7] Department of Electrical and Computer Engineering, University of Southern California, Los Angeles, CA, USA
[8] Center for Spatial Perception and Concrete Experience, University of Southern California, Los Angeles, CA, USA

[*] Current address: Sandia National Laboratories, New Mexico, USA
[**] Current address: Physical Medicine and Rehabilitation, Johns Hopkins University, Baltimore, MD, USA

[#] Corresponding authors: J. Joshua Yang (jjoshuay@usc.edu), Sergei Gepshtein (sergei@salk.edu), Alexander G. Balanov (a.balanov@lboro.ac.uk), Sergey E. Savel'ev (s.saveliev@lboro.ac.uk)

Abstract

Rapid development of memristive elements emulating biological neurons creates new opportunities for brain-like computation at low energy consumption. A first step toward mimicking complex neural computations is the analysis of single neurons and their characteristics. Here we measure and model spiking activity in artificial neurons built using diffusive memristors. We compare activity of these artificial neurons with the spiking activity of biological neurons measured in sensory, pre-motor, and motor cortical areas of the monkey (male) brain. We find that artificial neurons can operate in diverse self-sustained and noise-induced spiking regimes that correspond to the activity of different types of cortical neurons with distinct functions. We demonstrate that artificial neurons can function as trans-functional devices (*transneurons*) that reconfigure their behaviour to attain instantaneous computational needs, each capable of emulating several biological neurons.

It is unlikely that hardware emulation of the whole biological brain can be realised in the near future. But emulation of reduced models of the brain appears to be within reach [1-3], offering much-needed insight into information processing in biological neural systems and opening new avenues for artificial intelligence. In accord with the neuron doctrine in neuroscience [4], the first step toward understanding complex neural computations is the analysis of single neurons and their characteristics, such as receptive fields and response fields.

The concepts of receptive field and response field have played a key role in neurophysiology [5], helping to understand how the brain processes information (Fig. 1). To the physicist, this concept is reminiscent of the concept of mean field, where interactions among many particles in an ensemble are approximated by an effective field acting on a pseudo-particle, representing the collective behaviour of real particles. Similarly, the interactions among neurons in a network are represented by the receptive/response field of a single neuron, enabling prediction of the collective activity of neural populations [5-6]. Here we use artificial memristive neurons to emulate activity of biological neurons in functionally different parts of the brain.

Memristors are among the most promising technologies for emulating [7-9] brain activity, which are used to develop artificial neurons and synapses in hardware [10]. These electronic circuit elements have a resistance that depends on the history of electrical stimulation. Defined axiomatically by Chua [7] and implemented in a physical device by Williams et al. [8-9], the invention of memristors spurred the development of a broad family of classical and quantum elements [11-12]. The state of these elements depends upon the history of current and voltage in electric circuits, paving the way for future reconfigurable electronics capable of surpassing Moore's scaling limits, emulating the human brain, and enabling powerful analog CMOS-integrated computing hardware [13-14].

Among the various prior realisations of artificial neurons, whether using memristive [15-17] or non-memristive elements [18-20], the overwhelming majority are designed to respond to electric stimulation by generating *deterministic* spiking (e.g., [17, 21-22]). In contrast, biological neural systems are intrinsically *stochastic* due to random chemical and electrical fluctuations, as well as noisy inputs from other neurons originating in their complex dynamics within the network. If artificial neuromorphic hardware fails to accurately emulate the stochastic behaviour of biological neurons, it may struggle to achieve brain-level performance in solving diverse optimization problems [23]. Additionally, artificial neurons may be unable to replicate certain brain functions [24–26] that critically depend on stochastic dynamics. While it is well known that the complex dynamics of memristive neurons can produce a variety of spiking regimes [21-22], it remains unclear whether memristive neurons can mimic the stochastic dynamics of various types of neurons in the living brain.

In the following, we investigate the behaviour of inherently stochastic artificial neurons built using diffusive memristors and compare it with spiking activity of neurons in different regions of the brain cortex in awake animals (Fig. 1). These cortical regions participate in various cognitive functions, including the analysis of visual stimulation and the planning and control of hand movement. Despite the functional differences, the operations and information processing conducted by neurons in these different cortical regions share significant similarities. For instance, these neurons exhibit selectivity, i.e., they boost responses to certain features of stimulation or types of movement (Fig. 1 insets).

To compare the properties of biological neurons with their artificial counterparts, we use artificial neurons based on diffusive memristors. In these devices, clusters of Ag atoms ("Ag clusters," Fig. 2B-C) diffuse between electrodes to form conducting filaments. The formation and rupture of these filaments are responsible for switching of the neuron's conductance [27-29]. We observe distinct spiking patterns in measurements of the artificial neuron and perform stochastic simulations of artificial diffusive neurons to reveal their distinct dynamical regimes. These regimes are associated with self-sustained or noise-induced spiking that drives the neurons' selective responses to

stimulation. We then confirm all the predicted dynamical regimes in experiments with fabricated artificial neurons and compare the activity of these artificial neurons with the activity of biological neurons measured in three distinct cortical areas in awake macaque monkeys (Fig. 1). We find that a single artificial neuron can emulate the stochastic spiking behaviour of biological neurons in each studied cortical area by tuning the applied voltage, bath temperature and/or parameters of the neuromorphic circuit responsible for the characteristic time of artificial neuron (Fig. 2A).

We also demonstrate that artificial neurons exhibit more intense spiking response at their "natural" frequencies, revealing frequency selectivity regulated by stimulation intensity, closely analogous to the biological selectivity observed in neurons of the visual cortex [6]. Additionally, we show how a single transneuron can process two signals simultaneously and perform phase detection by leveraging the dynamical multistability of its spiking regimes. This is evidence that a single artificial neuron can perform tasks that would typically require several biological neurons. We introduce the term "transneuron" to indicate that the same physical device – an artificial neuron – can transition between the spiking characteristics of different types of biological neurons (Fig. 2A).

Noise-induced and self-sustained spiking in artificial diffusive neurons

We fabricate diffusive memristors and use them to build transneurons (Fig. 2B-C), in which we measure their responses to input voltages (Methods). When a DC voltage above a certain threshold is applied, the artificial neuron generates spikes of current, which are similar to the spiking activity of biological neurons. To understand the spiking mechanisms of an artificial neuron, we simulate transneuron spiking dynamics using stochastic differential equations [Eqs. (1a)-(1c); and Section 1 in Supplementary Information (SI)].

We investigate different spiking modes in artificial neurons by analysing how spiking depends on circuit parameters as well as external voltages and temperatures (Fig. 3). As we change the DC voltage, we observe dynamical patterns of current spikes that manifest different degrees of stochasticity. The experimentally observed spiking patterns range from quite regular to noisy, or to repetitive spike trains, as shown in the different columns of Fig. 3. These patterns typically occur within specific intervals of input voltages, beginning at a certain threshold voltage, intensifying as the voltage increases, and then diminishing or disappearing at higher voltages (Fig. 3A-E or 3F-J). Changes in temperature also influence spiking, making the patterns noisier and/or more intense. Adjusting either the input voltage or the load resistance can lead to qualitative changes in the spiking pattern, such as transitions from regular spiking to spike trains.

For example, first consider measurement of transneurons stimulated by long pulses of a constant (DC) voltage (Figs. 3-4). At low DC bias voltage, no spiking is observed. As the voltage increases, the system first generates rare and random spikes, and then it evolves toward a regular spiking mode (Fig. 3A-C). A comparison of the measurement results and stochastic simulations is shown in Figs. 4A and 4D, respectively. This quite regular spiking regime persists in simulations even when the random noise in the system is completely suppressed. Indeed, our bifurcation analysis shows (see SI section 3 and Fig. S1) that regular spiking occurs in this regime because the system develops a limit cycle via an Andronov-Hopf bifurcation at a certain threshold voltage $V = V_{th1}$. A gradual increase in spiking intensity, as observed in our stochastic simulations and experiments (Figs. 3-4), is consistent with this dynamical mechanism.

As voltage increases further, spiking becomes sparse and irregular again (see results of measurements in Figs. 3D,E and Fig. 4B and stochastic simulations in Fig. 4E), consistent with the dynamical mechanism of disappearance of the limit cycle at the second Andronov-Hopf bifurcation at $V = V_{th2}$. Intriguingly, more intense and fairly regular spiking reappears at even higher voltages, shown in Fig. 4C for measurements and in Fig. 4F for stochastic simulations. In contrast to the regular spiking regime at lower voltages, this spiking regime does not arise if the contribution of noise in Eq. (1a)-(1c) is

ignored. This fact suggests that heat can generate pseudo-deterministic forces due to thermophoresis and/or Seebeck effects [30-31], which produce a new limit cycle.

A simple deterministic model [Eqs. (2a)-(2d)] accounts for the temperature-gradient forces and successfully predicts results of both stochastic simulations and experimental measurements of the appearance of the second spiking regime. The bifurcation analysis of these deterministic equations reveals an additional dynamical spiking mechanism, originating from a distinct limit cycle that emerges through a nonlocal bifurcation at higher voltages, complementing the regular (periodic) oscillations observed at the lower voltages. The physical mechanisms underlying these two distinctive spiking regimes observed at low and high voltages differ: low-voltage oscillations result from the charging and discharging dynamics of circuit capacitance, whereas high-voltage oscillations stem from the slower heating and cooling cycle [32].

To evaluate the degree of stochasticity and regularity in these spiking regimes, we compare the power spectral density of the electrical current spikes observed in our simulations and measurements at three different voltages (measurements shown in Fig. 4G and simulations in Fig. 4H). At low voltages, the current spectral density exhibits clear maxima at specific frequencies, indicating the characteristic oscillation period (and harmonics) of the artificial neuron. At intermediate voltages, the spectral maximum is suppressed, reflecting an irregular response with significant contributions across a wide range of frequencies. At high voltages, prominent but broad maxima reappear, indicating self-sustained yet noisy spiking.

Next, we vary the voltage slowly and linearly over time, in contrast to the previously described DC voltage pulses. This slow sweep of voltage reveals that spiking patterns transition smoothly between regimes, indicating that the level of stochasticity can be precisely controlled within the same device by adjusting the bias voltage. These results are shown for measurements in Fig. 4I and for simulations with two identical Ag-clusters in Fig. 4J (see section 3 in SI): spiking at low voltages, which shows quite regular pattern, is replaced by spike trains at higher voltages. Such spike trains are similar to the activity pattern commonly observed in biological neurons [33] (section 5 in SI); their evolution with voltage is illustrated in Fig. 3F-J.

Transneurons emulate visual, motor and pre-motor neurons in the monkey brain

First, we compare the dynamics of artificial neurons with the spiking activity of biological neurons in two areas of the cerebral cortex – the middle temporal (MT) and parietal reach region (PRR) – in behaving rhesus monkeys. Neurons in these areas are known for their specialization: they exhibit selectivity for visual stimuli in the MT area of visual cortex [34-35] and control for directed arm movements in the functionally defined PRR [36-37] (Fig. 1). In both sensory (MT) and motoric (PRR) areas, we measured spiking activity of individual neurons while monkeys performed a behavioural task (see Methods for details).

We evaluate stochastic properties of spiking activity in these cortical areas using two metrics [38]. One is the coefficient of variation CV_1, which is the ratio of the standard deviation of inter-spike intervals (ISI) to the mean ISI. CV_1 is an index of stochasticity across the *entire duration* of the trial; it reveals the amount of periodicity in the system dynamics, and it quantifies the amount of irregularity generated by noise. For example, enhancement of stochasticity increases the standard deviation of ISI and thus yields a larger value of CV_1.

The second metric is the coefficient of variation CV_2, which is an index of *local* variability (or local time correlations) of spiking activity. We estimate CV_2 by first calculating the value of $2\,|\Delta t_{n+1} - \Delta t_n|/(\Delta t_{n+1} + \Delta t_n)$, where n denotes the spike serial number and Δt_n is the inter-spike interval separating $(n+1)\,th$ and nth spikes; we then average the results over the duration of the trial. This metric ($0 \le CV_2 < 2$ by definition) is used widely for the analysis of spiking in different parts of the brain

[38]; it describes correlations in sequential inter spike intervals (ISIs) and it is useful for quantifying persistence of ISI changes. The lower the value of CV_2 the more persistent the correlations in the sequence of ISIs, allowing for more reliable readout of the encoded information. However, the lower CV_2 the less information can be stored in ISI sequences, suggesting that information processing is most efficient at intermediate values of CV_2. For the studied transneurons, our analysis shows that CV_2 can be tuned over a broad range between 0.1 and 1.9 (Fig. 5A), thus offering significant flexibility for task-specific computational needs. Nevertheless, to understand what values of CV_2 optimise task-specific information processing, one should consider specific computational protocols, larger neural networks, and various readout mechanisms (not studied here).

In Fig. 5A, we plot CV_1 and CV_2 metrics against one another for multiple MT (yellow squares) and PRR (green diamonds) neurons. The plot reveals that clusters of $(CV_1,\ CV_2)$ points that correspond to spiking activity of MT and PRR neurons occupy different regions in this parameter space. This finding reveals different stochasticity and sensitivity to stimulus excitation in these cortical areas. We find that these stochastic characteristics are not significantly affected by stimulus intensity indicating that they are mainly intrinsic to neurons (Fig. S5 in section 7 of SI). In Fig. 5A we also plot the $(CV_1,\ CV_2)$ points obtained from numerical simulations (grey hexagons) of our transneuron stochastic model and measurements from artificial neurons (small black circles) across various load resistance and DC voltage values. The hammer-like shape of the simulated $(CV_1,\ CV_2)$ cloud closely resembles the shape of the region occupied by the measured $(CV_1,\ CV_2)$ points of transneurons. The simulated and measured data for transneurons overlap significantly with the data representing the activity of biological neurons in areas MT and PRR. Specifically, the convex hull of $(CV_1,\ CV_2)$ points for transneurons measured at different external voltages, resistances, and capacitances, shown in Fig S6, covers about 70% of PRR $(CV_1,\ CV_2)$ points and 100% of MT $(CV_1,\ CV_2)$ points. Additionally, we simulated spiking activity to estimate $(CV_1,\ CV_2)$ characteristics under varying noise intensities (see section 4 of SI). The results show that a modest increase in noise shifts the $(CV_1,\ CV_2)$ point distributions, causing only a minor reduction in the overlap between the $(CV_1,\ CV_2)$ distributions of biological neurons and transneurons.

The significant overlap of the *measured* $(CV_1,\ CV_2)$ points for the transneuron with the $(CV_1,\ CV_2)$ clouds for MT and PRR neurons is evidence that tuning the load resistance and DC voltage applied to the artificial neuron can produce distinct stochastic spiking activities that emulate the behaviour of these biological neurons. Such tunability arises from the competition between several dynamical attractors, each affected differently by noise and characterized by distinct basins of attraction. The multiple bifurcations observed in transneurons can be associated with the phenomenon of "edge of chaos" [39], highlighting their remarkable capacity for dynamic reconfiguration.

The finding that transneurons can produce spiking with CV_1 values even higher than the typical range for MT neurons, albeit with lower CV_2, suggests another type of spiking behaviour characterised by a combination of high persistence in successive ISIs and high overall randomness. We expect such behaviour from bursting neurons [33]. To explore this hypothesis, we analyse transneuron dynamics across a broader parameter range than above, including the temperature dependence of spiking (see Fig. 3N-O for an example). As predicted, we find a distinct patterns of bursting activity (Fig. 3F-J). Notably, increasing the bath temperature results in noisier bursting, characterised by shorter and more irregular quiet intervals (see Fig. S2 in section 5 of SI). Additionally, by varying the external voltage, we observe that bursting occurs only within a specific voltage range (Fig. 3F-J), allowing the bursting regime to be switched on or off, or even tuned to specific inter-train interval values.

We compare these results with the bursting activity of biological cortical neurons recorded in the monkey premotor cortex (PM) using publicly available spiking data [40]. Intensive spiking activity ("bursting") alternates with quiet intervals in both biological PM neurons (Fig. 2A, S3A), measured transneurons (e.g., Fig 3F-J), and simulated transneurons (Fig. 5D, S2B-C) within a specific window of

external voltages. We add the (CV_1, CV_2) points for bursting PM neurons to Fig. 5A (orange triangle), revealing significant overlap with the simulated and measured (CV_1, CV_2) points for artificial transneurons. Indeed, the convex hull of the measured $(CV_1,\ CV_2)$ points for transneurons covers 100% of PM $(CV_1,\ CV_2)$ points (see Fig. S6 in SI). This finding suggests that transneurons can also emulate features of spiking activity in the PM cortex.

Next, we demonstrate that by setting specific values for the load resistance and capacitance of the transneuron, and varying the external voltage within a certain range, it is possible to target a preselected region of the (CV_1, CV_2) stochastic characteristic. For example, the measured (CV_1, CV_2) points for a transneuron with a load resistance of 65kOhm and an external capacitance of 1 nF, when the external voltage varies between 0.6V and 0.8V, fall within the (CV_1, CV_2) region corresponding to the stochastic behaviour of MT neurons (Fig. 5A1). This demonstrates that, within this external voltage range, the transneuron accurately mimics the spiking behaviour of MT neurons, with its stochastic features remaining stable despite modest voltage variations. The distribution of yellow and black points suggests that these voltage variations enable the transneuron to exhibit stochastic activity encompassing the entire (CV_1, CV_2) cloud.

To complete the comparison of stochasticity between the transneuron and biological neurons, Fig. 5A2 shows that a transneuron with a load resistance of 70KOhm and an external capacitance of 100 nF exhibits a gradual drift in the measured (CV_1, CV_2) points between distinct (CV_1, CV_2) regions corresponding to different types of biological neurons. These transneuron points shift from the region corresponding to PRR neurons to the region corresponding to PM neurons as the voltage changes from 1.06V to 1.22V. Specifically, half of the measured transneuron (CV_1, CV_2) points for the same neuron fall within the PRR cluster, while the other half fall within the PM cluster. This highlights the transneuron's ability to emulate biological neurons from different cortical areas by simply varying the external voltage applied to the same fabricated device.

Maps of stochastic characteristics, such as the map of CV_1 and CV_2, are instrumental for identifying circuit parameters and DC voltage settings that enable artificial neurons to emulate the stochastic characteristics of specific types of biological neurons, producing the desired response. For instance, Fig. 5B shows the simulated CV_1 as a function of load resistance (R_{ext}) and external voltage (V_{ext}). The artificial neurons replicate the spiking statistics of PRR neurons at lower V_{ext} and R_{ext} values, corresponding to the first spiking regime (Fig. 4A, D). At higher voltages, where noisy bursting occurs in the second spiking regime (Fig. 4C, F), the CV_1 values of artificial neurons align with those of PM neurons (see timestamps in Fig. S3A in SI). MT-like behaviour in artificial transneurons is observed at both higher voltages and higher resistances.

Finally, to visualise spiking patters in different regions of the $(CV_1,\ CV_2)$ space, we present examples of simulated spiking conductance in Fig. 5C-E. These examples correspond to specific $(CV_1,\ CV_2)$ points selected from Fig. 5A, whose stochastic characteristics represent PRR, PM, and MT neurons.

Transneuronal computations

Biological and digital information processing follows different computational principles. Digital processing is implemented by sequences of logic gates applied to digitized information. Biological processing involves parallel spiking activity elicited by analogue stimulation [41], which is sequentially filtered and followed by decision-making. Instead of logic gates, neural computations are mediated by filtering mechanisms [42], where selectivity is reflected in the spiking activity that is enhanced or suppressed depending on the stimulus content. This dynamics modifies synaptic connections between neurons, enabling the system to encode past experiences and forming the basis for learning [43-44]. While synaptic weight adjustment has been implemented in artificial neural networks, here we focus on two other aspects of neural computation: (a) information processing through selective response to

stimulation and (b) transitions between coexisting dynamical regimes. Both these aspects can be realised within a single artificial transneuron.

Computation by selectivity

We investigate the selectivity of artificial neurons by applying a voltage signal $V_{ext}\ (t)$ comprising both DC and AC components ($V_{ext} = V_{DC} + V_{AC}\cos\omega t$, shown as blue curves in Fig. 6A-B) and measuring as well as simulating the electrical current response (red curves in Fig. 6A-B). DC and AC components of the signal allow one to (i) mimic the neuron's rest state (with spontaneous or non-stimulus-induced spiking activities) via DC voltage input, V_{DC}, and (ii) supply stimulus information via the frequency content of the AC signal, $V_{AC}\cos\omega t$. We first analyse the neuron's spiking behaviour as a function of the stimulus frequency (ω) at a fixed stimulus magnitude (V_{AC}), which corresponds to stimulus intensity. This experimental approach draws inspiration from a common method used to measure the selectivity of visual cortical neurons, employing windowed drifting luminance gratings as optical stimuli [35].

To track the evolution of ISI distributions (Figs. 6C-D), we accumulate spiking statistics over time. This approach is analogous to information gathering in biological diffusion-decision models [26]. The colour map in Figs. 6C-D depicts the probability density of ISIs as a function of the AC stimulus period ($t_p = 2\pi/\omega$), which is the inverse of stimulus frequency. The red, white, and blue colours represent the respective high, medium, and low probability densities, respectively. The dotted green curve marks the most probable ISI, while the yellow dashed line indicates the ISI value matching the stimulus period. Over the range of the t_p values close to the reciprocal of the neuron's natural spiking frequency (140 Hz at 1V for the fabricated transneuron with $V_{AC} = 0$), the peak of the ISI distribution aligns with the stimulus period. Within this range, the ISI distribution narrows and exhibits a higher peak compared to when t_p is away from the inverse of the natural spiking frequency. This behaviour reflects the neuron's frequency selectivity (see red regions in the measured and simulated 2D histograms in Figs. 6C-D). Such a selective activation of the transneuron resembles the phenomenon of synchronisation [45] observed in deterministic oscillator-based computation [46]. In our case selective activation is realised in an essentially stochastic system.

To clarify the relationship between stochastic synchronisation in transneurons and the selectivity of biological neurons, we note that the selectivity of biological neurons is typically determined by identifying the stimulus feature that elicits the maximum firing rate in response to a particular feature of the stimulus (Fig. 1). In Fig. 6E, we plot the firing rate of an MT neuron against the time-oscillation period (t_{MT}) of a visual stimulus (drifting luminance grating) at various luminance contrasts. The spike rate peaks at a specific value of t^*_{MT}, representing the neuron's preferred temporal frequency [6, 33]. Interestingly, the preferred time-period (t^*_{MT}) shifts toward lower values as the stimulus contrast increases, mirroring the previously observed shift in the preferred spatial frequency of these neurons [6, 35].

To compare selectivity of biological neurons with selectivity of artificial neurons, we plot the spike rate of transneurons as a function of the AC-voltage time period (here representing the intensity of simulation, analogous to the luminance contrast of visual stimulation of MT neurons). Similar to biological neurons, the spike rate of transneurons reaches a maximum (Fig. 6F-G) at a specific voltage oscillation period, t^*_p. Notably, both experimental data (Fig. 6F) and simulations (Fig. 6G) show a sharpening of the ISI distributions (Fig. 6C-D) for t^*_p, where the maximum spiking rate is observed. Longer spiking sequences recorded in simulations reveal a shift in the maximum spiking rate as the AC-voltage amplitude (V_{AC}) increases. Specifically, t^*_p shifts to lower values with increasing V_{AC}, mimicking the shift of t^*_{MT} in MT neurons with increasing stimulus contrast (Fig. 6E). This finding highlights even deeper similarities in the nonlinear spiking regimes of transneurons and biological neurons, extending beyond the so-called classical concept of receptive field, despite significant

structural and parametric differences. These include: (a) visual stimulation does not directly excite MT neurons but rather through several intermediary stages in the neural visual pathways, and (b) the temporal frequency of visual stimulation is significantly lower than the spiking frequency of MT neurons.

Computation by signal comparison

Signal comparison, particularly phase comparison, is widely used in biological systems. Notable examples include the computation of binocular disparity, which supports stereoscopic vision [47], and the computation of the speed of moving visual stimuli [48]. Signal comparison also plays a key role in many higher-order information processing tasks [49-50]. Beyond biological systems, signal comparators are extensively used, e.g., in communication technologies [51] and interferometry [52].

Here we propose a new computational approach for comparing the relative phases of two signals, leveraging the artificial neuron's ability to dynamically change its function during information processing. Specifically, we demonstrate how reconfiguring the dynamical regimes of spiking activity enables efficient multi-signal analysis. To explore how input voltage governs the "transitions" between distinct dynamical states in the one-Ag-cluster transneuron model, we present a phase diagram of the spiking regimes obtained for both stochastic [Eqs. (1a)-(1c)] and deterministic [Eqs. (2a)-(2d)] sets of equations in Fig. 7A. The figure illustrates the time evolution of Ag-particle position (x), which determines the memristor's conductance as the external voltage (V_{ext}) changes slowly. Simulation results for the stochastic and deterministic equations are shown as light grey and orange lines, respectively. The position (x) represents the location of the Ag nanoparticle cluster within the gap separating the tip of the nearly completed conducting filament from the memristor electrode (see section 1 in SI). The trajectory of $x(t, V_{ext}(t))$ exhibits hysteresis behaviour (dynamical multistability) as the applied voltage V_{ext} first increases and then decreases. Hysteresis occurs because bifurcation depends not only on the external conditions (e.g., voltage or temperature) but also on the ''system trajectory,'' which is determined by dynamical variables such as Ag-cluster location or local voltage. For this reason, when the applied voltage increases from the state where the Ag-cluster is attached to the tip of the filament, the system follows a different sequence of bifurcations compared to when the applied voltage decreases, and the Ag-cluster returns from the equilibrium position near the memristor terminal to the pillar tip. This complex dynamics results in two distinct regions (labelled I and III in Fig. 7A), each corresponding to a characteristic self-sustained spiking regime. These regions are separated by regions of noise-induced spiking (labelled II and IV in Fig. 7A), where the particle fluctuates either near one edge of the gap or near an equilibrium point of the system.

From these simulations and the bifurcation analysis, we conclude that within a specific range of external voltages (V_{ext}), the spiking regime coexists with the non-spiking (noise-induced) regime of Ag-cluster fluctuations (e.g., the voltage interval corresponding to the overlap of regions I and IV, indicated by the blue arrow in Fig. 7A). This multistability allows information to be stored in the coexisting dynamical states. Information stored in such states can be processed by switching between these states, as illustrated by the hopping indicated by the dark red arrow in Fig. 7A. This switching between spiking and non-spiking dynamics is triggered by thermal noise, whose intensity depends on the temperature. As noise increases, the likelihood of the Ag particle escaping its current dynamical state rises. To quantify this escape, we define the residual times the system spends either near the fixed point (non-spiking) or in the self-sustained limit cycle (intense spiking). These residual times determine the average spiking rate and are influenced by both temperature and external voltage.

To clarify the mechanism governing switching between different spiking regimes, we analyse how the basins of attraction for distinct dynamical states change with applied voltage when the system is in the metastable region. Using deterministic equations (2a-d), we simulate the system and find that the transneuron dynamics in the absence of noise are drawn either to the equilibrium point or the limit cycle, depending on the initial position of the Ag particle, $x(t = 0) = x_0$ (see Fig. S1C in SI). The

boundary separating regions of initial positions that lead to either spiking or non-spiking dynamics is formed by stable manifolds of the unstable equilibrium points. In the bifurcation diagram (Fig. 7A), this boundary is indicated by black dots $x_0(V_{ext}) = x_c(V_{ext})$ (unstable fixed points), which separate the basins of attraction for the two stable solutions. The larger is the basin of attraction, the greater the noise required for the system to switch to another state. The applied voltage controls the size of these basins (e.g., the basin of the equilibrium point disappears at the left tip of the dark blue horizontal arrow in Fig. 7A), while the temperature determines the intensity of the noise driving transitions between basins. For example, consider the moment when the applied voltage settles the transneuron in an equilibrium (non-spiking) state with a small basin of attraction. If the temperature is high at the same moment, the probability of switching to another state is high, reducing the transneuron's residual time in that state. In contrast, if the temperature is low at this moment, the Ag-cluster is more likely to remain in this non-spiking state, leading to a longer residual time. However, when the voltage settles the transneuron in an equilibrium state with a large basin of attraction, temperature becomes much less relevant, as even high noise (temperature) is unlikely to switch the transneuron to another spiking mode. This interplay between the voltage-controlled size of the basin of attraction and the temperature-controlled noise intensity demonstrates how two signals, encoded in the $V_{ext}(t)$ and $T_0(t)$ time series, influence the transneuron's residence times in either intensive or rare spiking states. As these residence times determine the average spiking rate, this analysis establishes a direct connection between the two input time signals and the average spiking intensity.

The preceding analysis of bifurcation mechanisms underlying distinct nanocluster dynamics demonstrates how various dynamical states and the control of transitions between them could be harnessed to develop a neuromorphic two-signal phase comparator (a "phase detector") using a single transneuron. Two input signals can be encoded in the external voltage $V_{ext}(t) = V_{DC} + V_{AC}\sin\omega t$ [the first time-dependent signal], and the bath temperature, $T_0(t) = T^*(1 + a_T\sin(\omega t + \phi))$ [the second signal]. For $V_{DC} - V_{AC}$ within the region of multistability (indicated by the blue horizontal arrow in Fig. 7A), the spiking intensity (Fig. 7B) depends on the relative phase ϕ, which is essential for phase detection. The spike rate (the computational output) reaches a minimum when the two signals are in phase ($\phi = 0$) and a maximum when the signals are in antiphase ($\phi = \pi$) (Fig. 7C-F). This behaviour reflects an interplay between noise-induced and self-sustained spiking. To qualitatively interpret this dependence, we need to examine the temperature at specific time points when the basins of attraction for (i) non-spiking and (ii) spiking states become very small, allowing noise to trigger an escape from these regimes. When the temperature and the external voltage oscillations are in antiphase, thermal noise promotes the system's transition into the self-sustained spiking regime [the low branch of $x(t, V_{ext})$ in the multistability region in Fig. 7A]. Indeed, for antiphase signals, the external voltage has the lowest value ($V_{ext} = V_{DC} - V_{AC}$) when the temperature is at its maximum [$T_0(t) = T^*(1 + a_T)$]. If the system at this instant resides in a non-spiking state (upper red branch in Fig. 7A), it is likely to switch to the spiking regime because the basin of attraction is small (due to low voltage) and the noise level is high (due to high temperature). Moreover, for $\phi = \pi$, when the voltage has its maximum value ($V_{ext} = V_{DC} + V_{AC}$), corresponding to the smallest basin of attraction in the spiking regime, the temperature is at its lowest. Therefore, the artificial neuron has a low chance of switching back to the non-spiking state because, even when the attraction region is small, the temperature is also low, reaching its lowest value $T_0(t) = T^*(1 - a_T)$, which produces insufficient noise for the transneuron to escape from the spiking state, switching back to non-spiking. This interplay of temperature-induced hopping between spiking regimes, on one hand, and the voltage-induced change in the basins of attraction for spiking states, on the other hand, causes the artificial neuron to remain in the spiking state significantly longer during antiphase (π-shift) oscillations of voltage and bath temperature. In contrast, for in-phase (0-shift) oscillations of external voltage and temperature, the same mechanism facilitates easier transitions from spiking to non-spiking regimes while suppressing reverse switching. Consequently, the transneuron spends much more time in the non-oscillating state when the phase shift is zero.

We conduct an experimental test to evaluate whether a single diffusive neuron can perform signal comparison. The neuron's spiking response is measured while varying the external voltage and background temperature in-phase (Fig. 7I) and anti-phase (Fig. 7J). The experimental results (Fig. 7G-H) closely match the simulations (Fig. 7C-D), demonstrating significantly more intense spiking during anti-phase oscillations of voltage and temperature compared to in-phase oscillations. For proof-of-concept, as shown here, the entire diffuse memristor was periodically heated. However, achieving energy efficiency would require localized heating, which could be implemented using several modern techniques. One of the most practical implementations of this concept could involve a nanoscale thin-film Joule heater [53]. Such systems could localize temperature oscillations to scales as small as a single memristor filament or even part of the filament. Since the heated region would be extremely small (potentially involving just a few Ag clusters), the required power consumption and related energy loss could be very low. Moreover, the signal encoded in temperature modulations could, in principle, be implemented using a near-field enhancer of the laser field, creating hotspots as small as 10 nm–100 nm [54, 55]. However, this approach would increase the complexity of fabricating transneurons and neuromorphic devices as a whole. The energy loss per signal cycle can be estimated as $C_{Ag}\rho_{Ag}N\ (4\pi r_{Ag}^3/3)\Delta T$, where C_{Ag} is the heat capacitance of silver, ρ_{Ag} is its density, r_{Ag} is the cluster radius, N is the number of clusters in the heated filament bottleneck, and ΔT is the temperature variation. Assuming $C_{Ag} = 0.236\ J/g$°C, $\rho_{Ag} = 10.49\ g/cm^3$, N = 10, r_{Ag} = 10 nm, and $\Delta T = 100$ °C, the required energy per oscillation is estimated to be 0.1 picoJoule. This corresponds to a potential power consumption as low as 10^{-5} Watt at a signal cycle frequency of 0.1 GHz.

Transneurons sensitive to the relative phase of two signals could facilitate the creation of compact circuits capable of analysing complex signals (see section 12 in SI). AI systems built with transneurons may surpass current AI hardware, paving the way for dynamical cognitive processors [56]. For instance, estimating the distance to objects typically requires at least two conventional sensory neurons, which respond to slightly shifted signals (e.g., acoustical or optical), connected to a decision neuron that computes distance by comparing their activity. This three-neuron circuit could be replaced with a single transneuron that receives paired stimuli, functioning as a hybrid of sensor and decision neuron. Furthermore, tuning a transneuron to operate at the boundary between self-sustained and noise-induced regimes could enable advanced coding schemes, where stimulus information is encoded in the distribution of ISIs rather than solely in the ISI rate (see section 10 in SI).

In conclusion, artificial neurons based on diffusive memristors can effectively emulate various types of biological neurons while supporting multiple coexisting spiking regimes within a single device. These features pave the way for future artificial intelligence systems with dynamical learning capabilities [56-58].

METHODS

PHYSIOLOGICAL STUDIES

Middle Temporal Cortical Area (MT)

Electrophysiological Recordings. Recordings were made in cortical areas MT in two adult male rhesus monkeys. Activity of single neurons was recorded using tungsten microelectrodes driven into cortex using a hydraulic micropositioner. Neurophysiological signals were filtered, sorted, and stored using the Plexon (Dallas, TX) system. Visual responses were recorded while the animals performed a fixation task. Firing rates were measured at five to seven different levels of luminance contrast in the vicinity of the neurons' preferred spatiotemporal frequencies. The different stimulus conditions and contrasts were interleaved in random order across trials. To compute population response (Fig. 5, 6), the firing rates of individual neurons (ranging from 20 to 100 spikes/sec) were normalized to their maximal firing rates [6]. See Section 13 of SI for additional recording details.

Behavioural procedure. Monkeys were seated in a standard primate chair with a surgically implanted head post rigidly affixed to the chair frame. The task was to fixate a small target in the presence of moving visual stimuli for the duration of each trial. The eye position was monitored and recorded. After eye position was maintained within a 2 deg window centred on the fixation target throughout the trial, animals were given a small juice reward. See Supplementary Materials for additional detail of procedure.

Parietal Reach Region (PRR)

Electrophysiological Recordings. Single-unit recordings were made from both hemispheres in each of two adult male rhesus monkeys. Boundaries of cortical area PRR were identified based primarily on physiological criteria. See Section 13 of SI for additional recording details.

Behavioural procedure. Animals first fixated on a circular white stimulus centred on the screen in front of them. Left and right paws touched "home" pads situated at waist height and in front of each shoulder. After holding the initial eye and hand positions, either one or two peripheral targets appeared on the screen. When two targets appeared, they were at opposite locations relative to the fixation point. After an additional period that lasted above 1 s, the central eye fixation target shrank in size to a single pixel, cueing the animal to move to the peripheral target(s) in accordance with target colour. Trials could be unimanual or bimanual. Animals were given a small juice reward on correct trials. See Supplementary Materials for additional detail of procedure.

Motor Cortex

Neuronal recordings were performed in macaque monkeys performing a delayed reach-to-grasp task using Utah Arrays implanted along the central sulcus and overlapping the border between primary motor cortex and dorsal or ventral premotor cortex of the right hemispheres of two rhesus monkeys as described in [40].

Experimental protocols were approved by the Animal Care and Use Committees of the Salk Institute and of the Washington University School of Medicine, and they conform to U.S. Department of Agriculture regulations and to the National Institutes of Health guidelines for the humane care and use of laboratory animals.

ARTIFICIAL NEURONS

Fabrication

Method 1: We fabricated the diffusive memristor devices used to obtained data for Figs. 3-7, S6, S8 on a p-type (100) Si wafer with 100 nm thermal oxide. The bottom electrodes were patterned by photolithography followed by evaporation and liftoff of ~20/2nm Pt/Ti. The ~10 nm thick SiO_2 dielectric layer was deposited at room temperature by reactively sputtering SiO_2 in Ar. A 4nm Ag layer was subsequently deposited using the same technique as the dielectric. The ~30 nm Pt top electrodes were subsequently patterned by photolithography followed by evaporation and liftoff processes. Electrical contact pads of the bottom electrodes were first patterned by photolithography and then subjected to reactive ion etching with mixed CHF_3 and O_2 gases.

Method 2: For measurements presented in Figs. 3, 5, 7, S2, and S6 the diffusive memristors were prepared by co-sputtering Ag, and SiO_2 in Ar at room temperature. Dielectric layer of nominal thickness 40 nm deposited by co-sputtering was sandwiched between 30 (20) nm bottom (top) Pt electrodes. The top electrodes were sputtered through a shadow mask.

Measurements

Electrical measurements described in Figs. 3-7 were performed using the Keysight 33622 A arbitrary waveform generator, the Keysight MSOX3104 mixed signal oscilloscope, and the Keysight B1530 WGFMU. Voltage pulses were applied by the Keysight 33622 A. The analogue oscilloscope channels were used to measure the voltages at the output of the function generator, and across the diffusive memristor. The current across the diffusive memristor was monitored using a 1.5kΩ resistor connected in series to the diffusive memristor while the voltage across it was being monitored by one channel of the oscilloscope. We used electrolytic capacitors (100nF) and general-purpose resistors (70kΩ).

Electrical measurements presented in Figs. 3, 5, and 7 were performed using the Keithley 4200SCS, Rigol arbitrary waveform generator DG4162, and PicoScope 5443D oscilloscope on an Everbeing probe station. Electrical connections to the memristor were made via tungsten probe tips. Voltage pulses were applied by the waveform generator, and the oscilloscope channels were utilised to measure the voltage output of the pulse generator and the voltage across the diffusive memristor, which was hosted on a temperature-controlled chuck. The temperature of the chuck was controlled using an Everbeing temperature chuck controller and an ATC chiller. For the spiking circuit, we used a range of resistances between 55-90 kOhms general-purpose resistor and a 50 nF electrolytic capacitor.

Simulations

To simulate spiking activities, we used the model, which describes the interplay of three key processes that govern charge transport: (i) Ag nanocluster diffusion in a dielectric medium, (ii) electron tunnelling between the terminals and the Ag clusters, and (iii) heat flow dynamics (see, e.g., [27-28, 59]). The agreement between results of our simulations and measurements (both shown in Fig. 4) is evidence that the model captures the essential dynamics of the system and thus it can be used to analyse mechanisms of spiking.

Controlling spiking behaviour in artificial neurons requires understanding the relationship between stochastic and deterministic components in their dynamics. This task is particularly challenging for the diffusive memristor, where interactions between thermal, nanomechanical and electrical degrees of freedom produce intriguing thermo-mechanical and thermo-electric dynamics coupled with the diffusive drift of Ag-clusters that form conducting filaments. The diffusion is controlled by the nanocluster temperature, which is in turn determined by a balance between Joule local heating generated by current through the memristor and cooling due to the heat sink to the substrate having bath temperature T_0 (Fig. 2B). The current and the corresponding voltage across the memristor is defined by Kirchhoff's circuit law (Fig. 2B), while the memristor resistance is governed by electron tunnelling through the Ag-clusters between memristor terminals.

For a nearly formed filament, the memristance is controlled by a few particles [60] in the gap between the filament tip and the electrode (Fig. S1B). In this case, the model equations read:

$$\eta \frac{dx_i}{dt} = -\frac{\partial U(x_i)}{\partial x_i} + q\frac{V}{L} - \sqrt{\eta D}\xi_i(t), \quad (1a)$$

$$\frac{dT}{dt} = \frac{V^2}{C_{th}R(x_1,\ldots x_N)} - \kappa(T - T_0), \quad (1b)$$

$$\tau \frac{dV}{dt} = V_{ext} - \left(1 + \frac{R_{ext}}{R(x_1,\ldots x_N)}\right)\mathrm{V} + \sqrt{D_V}\varsigma_V(t). \quad (1c)$$

Here, x_i is the position of the *i*-th mobile particle (Ag-cluster) diffusing within the gap of size L, η is the viscosity coefficient, U is the phenomenological electro-chemical potential in the gap with a minimum near the top of the filament (Fig. S1A in SI), and V is the voltage drop across the gap. We renumerate particles during simulations to always keep $x_i > x_{i-1}$. In this work, we consider the cases of either one or two Ag-particles in the gap (Fig. S1B in SI). In the case of one particle, the resistance of the memristor is

539 $$R(x_1) = R_t\left(e^{\frac{(L/2+x_1)}{\lambda}} + e^{\frac{(L/2-x_1)}{\lambda}}\right) = R(x) = R_0\cosh\left(\frac{x}{\lambda}\right),$$

540 and for two particles it is

541 $$R(x_1, x_2) = R_t\left(e^{\frac{(L/2+x_1)}{\lambda}} + e^{\frac{(x_2-x_1)}{\lambda}} + e^{\frac{(L/2-x_2)}{\lambda}}\right).$$

542 Here R_t is the tunnelling resistance amplitude, and λ is the effective tunnelling length [59]. For one
543 particle in the gap, the minimum resistance of the memristor $R_0 = 2R_t e^{L/2\lambda}$ occurs when the Ag-
544 cluster is in the middle of the gap ($x = 0$). In the following we remove the subindex 1 in x_1 to simplify
545 notation when modelling one Ag-particle in the gap. The Ag-particles are driven by an electrical force
546 qV/L with the induced effective cluster charge q; they diffuse inside the gap under the influence of a
547 random force. In general, q could depend on voltage and it can change its sign when voltage is
548 inverted [59]. To avoid these unnecessary complications, we therefore consider only the case of
549 $V_{ext} > 0$ and simplify the problem assuming a constant induced charge.

550 The noise affecting artificial neuron dynamics comes from two sources: (i) Brownian dynamics of Ag-
551 clusters and (ii) external voltage noise in the artificial neuron circuits. These two sources of noise have
552 counterparts in biological neurons: the noise due to diffusion of ions in ion channels and the noise in
553 signals coming from other neurons in the neural network, connected to the given neuron. The noise
554 due to diffusive dynamics of the Ag-clusters is modelled by Gaussian stochastic forces $\xi_i(t)$ which are
555 delta-correlated in time and statistically independent for each cluster. The intensity of random
556 fluctuations is controlled by the diffusion constant, which is proportional to the temperature $D =$
557 $2k_BT$. The temperature is governed by the Newton's cooling law, where the rate of heat transfer to
558 the sink is determined by the cooling constant κ and the background temperature T_0. We assume
559 that the source of heat is the Joule dissipation, linked to temperature via the thermal capacitance C_{th}.
560 We found that, in general, the model with two Ag-particles in the gap reproduces the current spiking
561 observed in experiments with artificial neurons better than the model with one Ag cluster in the gap.
562 However, the dynamics of the two-particles system is more difficult to interpret. Moreover, the
563 broader distribution of CV_2 observed in the artificial neurons fabricated using Method 2, and having
564 large values of CV_1, is better captured by the one-particle model. This observation suggests that the
565 conductive pillars with one or two Ag clusters that control bottleneck resistance both exist in our
566 diffusive memristors fabricated for this study. Here we use the two-particle model for the results
567 presented in Fig. 4, and the one-particle model in other simulations.

568 Fluctuations of voltage mimicking the noise from other neurons appear in the equation (Eq. 1c), which
569 describes the voltage drop V across the memristor when an external voltage $V_{ext}(t)$ is applied. This
570 equation is derived by applying the Kirchhoff current law to the circuit shown in Fig. 2B with the load
571 resistance R_{ext} and the circuit time constant $\tau = RC$. The neural network noise is added via random
572 external voltage fluctuations $\sqrt{D_V}\varsigma_V(t)$, where D_V is the intensity of voltage fluctuation and $\varsigma_V(t)$ is
573 the uncorrelated Gaussian noise with zero mean.

574 The model (Eqs. 1a-c) has been successfully used to describe stochastic dynamics of diffusive
575 memristors [27-29]. Here we use it to analyse different spiking regimes. To distinguish between noise-
576 induced and self-sustained spiking, we also develop a deterministic model (see justifications of this
577 model in section 1 in SI) where thermal fluctuations are replaced by additional deterministic forces
578 related to the thermophoretic and/or thermoelectric effects [30-31]:

579 $$\eta\frac{dx}{dt} = -\frac{\partial U}{\partial x} - q\frac{V}{L} - q_T T', \qquad (2a)$$

580 $$\frac{dT'}{dt} = \frac{2VV'R - V^2R'}{C_{th}[R(x)]^2} - \kappa T', \qquad (2b)$$

$$\tau \frac{dV}{dt} = V_{ext} - \left(1 + \frac{R_{ext}}{R(x)}\right) V, \qquad (2c)$$

$$\tau \frac{dV'}{dt} = -\left(1 + \frac{R_{ext}}{R(x)}\right) V' + \frac{R_{ext} R'}{[R(x)]^2} V, \quad (2d)$$

where T' and V'represent electric and thermal gradients in the gap, and we add a force proportional to T' and a "thermal charge" q_T determined by the thermophoresis and/or Seebeck coefficients. Normalisations of the Eqs. (1) and(2) are discussed in Section 2 of SI.

References

[1] Yu, Q., Tang, H., Hu, J., Chen, K.T. Neuromorphic Cognitive Systems. *Springer* (2017).

[2] Aimone, J.B. A Roadmap for Reaching the Potential of Brain-Derived Computing. *Advanced Intelligent Systems* **3**, 2000191 (2021).

[3] Ham, D., Park, H., Hwang, S., Kim, K. Neuromorphic electronics based on copying and pasting the brain. *Nature Electronics* **4**, 635 (2021).

[4] Barlow, H.B., Single units and sensation: A neuron doctrine for perceptual psychology? *Perception* **1**, 371-394 (1972).

[5] Hubel, D. H, and Wiesel, T. N. Brain and Visual perception: The story of a 25-year collaboration. New York, Oxford University press (2005).

[6] Gepshtein, S. Pawar, A., Kwon, S., Savel'ev, S., Albright, T.D., Spatially distributed computation in cortical circuits, Science Advances 8, abl5865 (2022).

[7] Chua, L. Memristor-The missing circuit element. *IEEE Transactions on Circuit Theory* **18**, 507 (1971).

[8] Strukov, D.B., Snider, G.S., Stewart, D.R., Williams, R.S. The missing memristor found. *Nature* **453**, 80 (2008).

[9] Yang, J.J., Matthew, D.P., Li, X., Ohlberg, D.A.A., Stewart, D.R., and Williams, R.S. Memristive switching mechanism for metal/oxide/metal nanodevices. *Nature Nano.* **3**, 429 (2008).

[10] Choi, S., Yang, J., Wang, G. Emerging Memristive Artificial Synapses and Neurons for Energy-Efficient Neuromorphic Computing. *Advanced Materials* **32**, 2004659 (2020).

[11] Romero, F.J., Ohata, A., Toral-Lopez, A., Godoy, A., Morales, D.P., Rodriguez, N. Memcapacitor and Meminductor Circuit Emulators: A Review, *Electronics* **10**, 1225 (2021).

[12] N. Shevchenko, S.N., Pershin, Yu. V., and Nori F. Qubit-Based Memcapacitors and Meminductors. Phys. Rev. Applied 6, 014006 (2016).

[13] Song, W., Rao, M., Li, Y., Li, C., Zhu, Y., Cai, F., Wu, M., Yin, W., Li, Z., Wei, Q., Lee, S., Zhu, H., Gong, L., Barnell, M., Wu, Q., Beerel, P.A., Chen, M S.-W., Ge, N., Hu, M., Xia, Q., Yang, J.J. Programming memristor arrays with arbitrarily high precision for analog computing. Science **383**, 903 (2024).

[14] Rao, M., Tang, H., Wu, J., Song, W., Zhang, M., Yin, W., Zhuo, Y., Kiani, F., Chen, B., Jiang, X., Liu, H., Chen, H.-Y., Midya, R., Ye, F., Jiang, H., Wang, Z., Wu, M., Hu, M., Wang, H., Xia, Q., Ge, N., Li, J., Yang, J.J. Thousands of conductance levels in memristors integrated on CMOS. Nature **615**, 823 (2023).

[15] Ignatov, M., Ziegler, M., Hansen, M., Petraru, A., Kohlstedt, H. A memristive spiking neuron with firing rate coding. *Front. Neurosci.* **9**, 376 (2015).

[16] Zhang, Y., Wang, Z., Zhu, J., Yang, Y., Rao, M., Song, W., Zhuo, Y., Zhang, X., Cui, M., Shen, L., Huang, R., Yang, J.J. Brain-inspired computing with memristors: Challenges in devices, circuits, and systems editors-pick. *Applied Physics Reviews* **7**, 011308 (2020).

[17] Zhang, X., Zhuo, Y., Luo, Q., Wu, Z., Midya, R., Wang, Z., Song, W., Wang, R., Upadhyay, N.K., Fang, Y., Kiani, F., Rao, M., Yang, Y., Xia, Q., Liu, Q., Liu, M., Yang, J.J. An artificial spiking afferent nerve based on Mott memristors for neurorobotics. *Nature Communications* **11**, 51 (2020).

[18] Abu-Hassan, K., Taylor, J.D., Morris, P.G., Donati, E., Bortolotto, Z.A., Indiveri, G., Paton, J.F.R., and Nogaret, A. Optimal solid state neurons. *Nature Communications* **10**, 5309 (2019).

[19] Mahowald, M., Douglas, R. A silicon neuron. *Nature* **354**, 515 (1991).

[20] Indiveri, G. et al. Neuromorphic silicon neuron circuits. *Front. Neurosci.* **5**, 73 (2011).

[21] Yi, W., Tsang, K.K., Lam, S.K., Bai, X., Crowell, J.A., Flores, E.A. Biological plausibility and stochasticity in scalable VO_2 active memristor neurons. *Nature Communications* **9**, 4661 (2018).

[22] Kumar, S., Williams, R.S., Wang, Z., Third-order nanocircuit elements for neuromorphic engineering. *Nature* **585**, 518 (2020).

[23] Aarts, E., and Korst, J., Simulated Annealing and Boltzmann Machines: A Stochastic Approach to Combinatorial Optimization and Neural Computing .Wiley; 1st edition (1988)

[24] Faisal, A.A., Selen, L.P.J., Wolpert, D.M. Noise in the nervous system. *Nature Reviews Neuroscience* **9**, 292 (2008).

[25] Uddin, L.Q. Bring the Noise: Reconceptualizing Spontaneous Neural Activity. *Trends in Cognitive Sciences* **24**, 734 (2020).

[26] Ratcliff, R., Smith, P.L., Brown, S.D., McKoon, G. Diffusion Decision Model: Current Issues and History. *Trends in Cognitive Sciences* **20**, 260 (2016).

[27] Wang, Z., Joshi, S., Savel'ev, S., Jiang, H., Midya, R., Lin, P., Hu, M., Ge, N., Strachan, J.P., Li, Z., Wu, Q., Barnell, M., Li, G.-L., Xin, H., Williams, R.S., Xia, Q., and Yang, J. Memristors with diffusive dynamics as synaptic emulators for neuromorphic computing, *Nature Materials* **16**, 101 (2017).

[28] Jiang, H., Belkin, D., Savel'ev, S., Lin, S., Wang, Z., Li, Y., Joshi, S., Midya, R., Li, C., Rao, M., Barnell, M., Wu, Q., Yang, J.J., Xia, Q. A novel true random number generator based on a stochastic diffusive memristor, *Nature Communications* **8**, 882 (2017).

[29] Wang, Z., Joshi, S., Savel'ev, S., Song, W., Midya, R., Li, Y., Rao, M., Yan, P., Asapu, S., Zhuo, Y., Jiang, H., Lin, P., Li, C., Yoon, J.H., Upadhyay, N.K., Zhang, J. Hu, M., Strachan, J.P., Barnell, M., Wu, Q., Wu, H., Williams, R.S., Xia, Q., Yang, J.J. Fully memristive neural networks for pattern classification with unsupervised learning, *Nature Electronics* **1**, 137–145 (2018).

[30] Wang, M., Bi, C., Li, L., Long, S., Liu, Q., Lv, H., Lu, N., Sun, P., Liu, M. Thermoelectric Seebeck effect in oxide-based resistive switching memory. *Nature Communications* **5**, 4598 (2014).

[31] Kumar, S., Wang, Z., Huang, X., Kumari, N., Davila, N., Strachan, J.P., Vine, D., Kilcoyne, A.L.D., Nishi, Y., Williams, R.S., Conduction Channel Formation and Dissolution Due to Oxygen Thermophoresis/Diffusion in Hafnium Oxide Memristors. *ACS Nano* **10**, 11205 (2016).

[32] Ushakov, Y., Balanov, A., Savel'ev, S. Role of noise in spiking dynamics of diffusive memristor driven by heating-cooling cycles. *Chaos, Solitons & Fractals* **145**, 110803 (2021).

[33] Rüdiger, K. and Gabbiani, F. Burst firing in sensory systems. *Nature Reviews Neuroscience* **5**, 13 (2004).

[34] Albright, T.D., Desimone, R., Gross, C. Columnar organization of directionally selective cells in visual area MT of the macaque. *Journal of Neurophysiology* **51**, 16 (1984).

[35] Pawar, A.S., Gepshtein, S., Savel'ev, S., Albright, T.D. Mechanisms of Spatiotemporal Selectivity in Cortical Area MT. *Neuron* **101**, 514 (2019).

[36] Snyder, L. H., Batista, A. P., and Andersen, R. A. Coding of intention in the posterior parietal cortex. *Nature* **386**, 167 (1997).

[37] Mooshagian, E., Holmes, C.D., Snyder, L.H. Local field potentials in the parietal reach region reveal mechanisms of bimanual coordination. *Nature Communications* **12**, 1 (2021).

[38] Maimon, G., Assad, J.A., Beyond Poisson: increased spike-time regularity across primate parietal cortex. *Neuron* **62**, 426 (2009).

[39] Brown, T.D., Kumar, S., and Williams, R.S., Physics-based compact modelling of electro-thermal memristors: Negative differential resistance, local activity, and non-local dynamical bifurcations. *Applied Physics Reviews* **9**, 011308 (2022)

[40] Brochier, T. et al. Massively parallel recordings in macaque motor cortex during an instructed delayed reach-to-grasp task. *Sci. Data* **5**, 1 (2018).

[41] Rabinovich, M.I., Afraimovich, V.S., Bick, C., Varonad, P. Information flow dynamics in the brain. *Physics of Life Reviews* **9**, 51 (2012)

[42] Allman, J. M., Baker, J. F., Newsome, W. T., and Petersen, S. E. Visual topography and function. In Multiple visual areas. *Humana Press*, pp. 171-185 (1981).

[43] Baudry, M., Thompson, R.F., Davis, J.L., Synaptic Plasticity: Molecular, Cellular, and Functional Aspects. *MIT Press* (2003).

[44] Song, S., Miller, K.D., Abbott, L.F., Competitive Hebbian learning through spike-timing-dependent synaptic plasticity. *Nature Neuroscience* **3**, 919 (2000).

[45] Balanov, A., Janson, N., Postnov, D., Sosnovtseva, O., Synchronization: From Simple to Complex. *Springer Series in Synergetics* (2009)

[46] Csaba, G., Porod, W. Coupled oscillators for computing: A review and perspective. *Appl. Phys. Rev.* **7**, 011302 (2020).

[47] La Chioma, A., Bonhoeffer, T., and Hübener, M. Area-specific mapping of binocular disparity across mouse visual cortex. *Current Biology* **29**, 2954 (2019).

[48] Eichner, H., Joesch, M., Schnell, B., Reiff, D. F., and Borst, A. Internal structure of the fly elementary motion detector. *Neuron* **70**, 1155 (2011).

[49] Khamechian, M.B., Kozyrev, V., Treue, S., Esghaei, M., Daliria, M.R. Routing information flow by separate neural synchrony frequencies allows for “functionally labeled lines” in higher primate cortex. *PNAS* **116**, 12506 (2019).

[50] Carr, C.E. Processing of temporal information in the brain. *Annual Review of Neuroscience* **16**, 223, 1993.

[51] Nisa' Minhad, K., Ibne Reaz, M.B., Md Ali, S.H. Investigating Phase Detectors: Advances in Mature and Emerging Phase-Frequency and Time-to-Digital Detectors in Phase-Locked Looped Systems. *IEEE Microwave Magazine* **16**, 56 (2015).

[52] Jiang, Y., Brower, D.L., Zeng, L., Howard, J. Application of a digital phase comparator technique to interferometer data. *Review of Scientific Instruments* **68**, 902 (1997).

[53] Mecklenburg, M., Hubbard, W.A., White, E.R., Dhall, R., Cronin, S.B., Aloni, S., Regan, B.C. Nanoscale temperature mapping in operating microelectronic devices, Science **347**, 629 (2015)

[54] Tang, X., Xu, S., Wang, X. Nanoscale Probing of Thermal, Stress, and Optical Fields under Near-Field Laser Heating, PLoS ONE **8**, e58030 (2013).

[55] Hong, M.H., Huang, S.M., Luk'yanchuk, B.S., Chong, T.C. Laser assisted surface nanopatterning, Sensors and Actuators A **108**, 69 (2003).

[56] Janson, N.B., Marsden, C.J., Dynamical system with plastic self-organized velocity field as an alternative conceptual model of a cognitive system. *Scientific Reports* **7**, 17007 (2017).

[57] Buonomano, D.V., Maass, W., State-dependent computations: spatiotemporal processing in cortical networks. *Nature Reviews Neuroscience* **10**, 113 (2009)

[58] Monaco, J.D., Rajan, K., Hwang, G.M. A brain basis of dynamical intelligence for AI and computational neuroscience, arXiv:2105.07284 (2021).

[59] Savel'ev, S.E., Marchesoni, F., Bratkovsky, A.M., Mesoscopic resistive switch: non-volatility, hysteresis and negative differential resistance. *European Physical Journal B* **86**, 501 (2013).

[60] Yi, W., Savel'ev, S.E., Medeiros-Ribeiro, G., Miao, F., Zhang, M.-X., Yang, J.J., Bratkovsky, A.M., Williams, R.S. Quantized conductance coincides with state instability and excess noise in tantalum oxide memristors. *Nature Communications* **7**, 11142 (2016).

[61] Pattnaik, D.P., Ushakov, Y., Zhou, Z., Borisov, P., Cropper, M.D., Wijayantha, U.W., Balanov, A.G. Savel'ev, S.E. Temperature control of diffusive memristor hysteresis and artificial neuron spiking. *Phys. Rev. Applied* **19**, 024065 (2023)

ACKNOWLEDGEMENTS

We would like to thank Prof. Qiangfei Xia for elucidating comments about the manuscript. This work was supported by the Engineering and Physical Sciences Research Council grant No. EP/S032843/1 (SES, PB), a National Eye Institute (NEI) Core Grant for Vision Research P30 EY019005 (TDA, SG), NEI grants 5R01EY012135 (LHS), R01 EY018613 (TDA, SG), R01-EY029117 (TDA, SG), NIBIB+NIMH grant 1R01EB028154 (LHS), the X-Grants Program of the President's Excellence Fund at Texas A&M University (RSW) , and Air Force Office of Scientific Research grant under contract no. FA9550-19-1-0213 (RM, JJY).

CONTRIBUTIONS. SES conceived the concept and coordinated writing the paper. SES and AB wrote the initial draft and performed stochastic (Eqs. 1a-c) and deterministic (Eqs. 2a-d) simulations. AB performed bifurcation analysis of equations (2a-d) for artificial neuron. SES, AB, SG, and RSW wrote the manuscript. SS, JJY and AB designed the experiment and analysed data obtained from artificial neurons. SG led, and SES and AB contributed to, the analysis of biological data. SES, SG, AB, PB, JJY, TDA, and LHS supervised experimental studies. RW and DP performed experiments on artificial neurons. ASP and EM obtained data from MT and PRR biological neurons, respectively. All authors contributed to discussion and editing of the manuscript. First four authors contributed equally to experimental studies reported in the manuscript.

ADITIONAL INFORMATION is provided in Supplementary Materials.

Competing interests. The authors declare that they have no competing interests.

Data and materials availability. All data needed to evaluate the conclusions of the study are present in the Main Manuscript and the Supplementary Materials. Data and computer code supporting the conclusions are provided in zip-files.

Inclusion & Ethics. The authors have carefully considered researcher contributions and authorship criteria of multi-region collaboration to promote greater equity in this collaborative project.

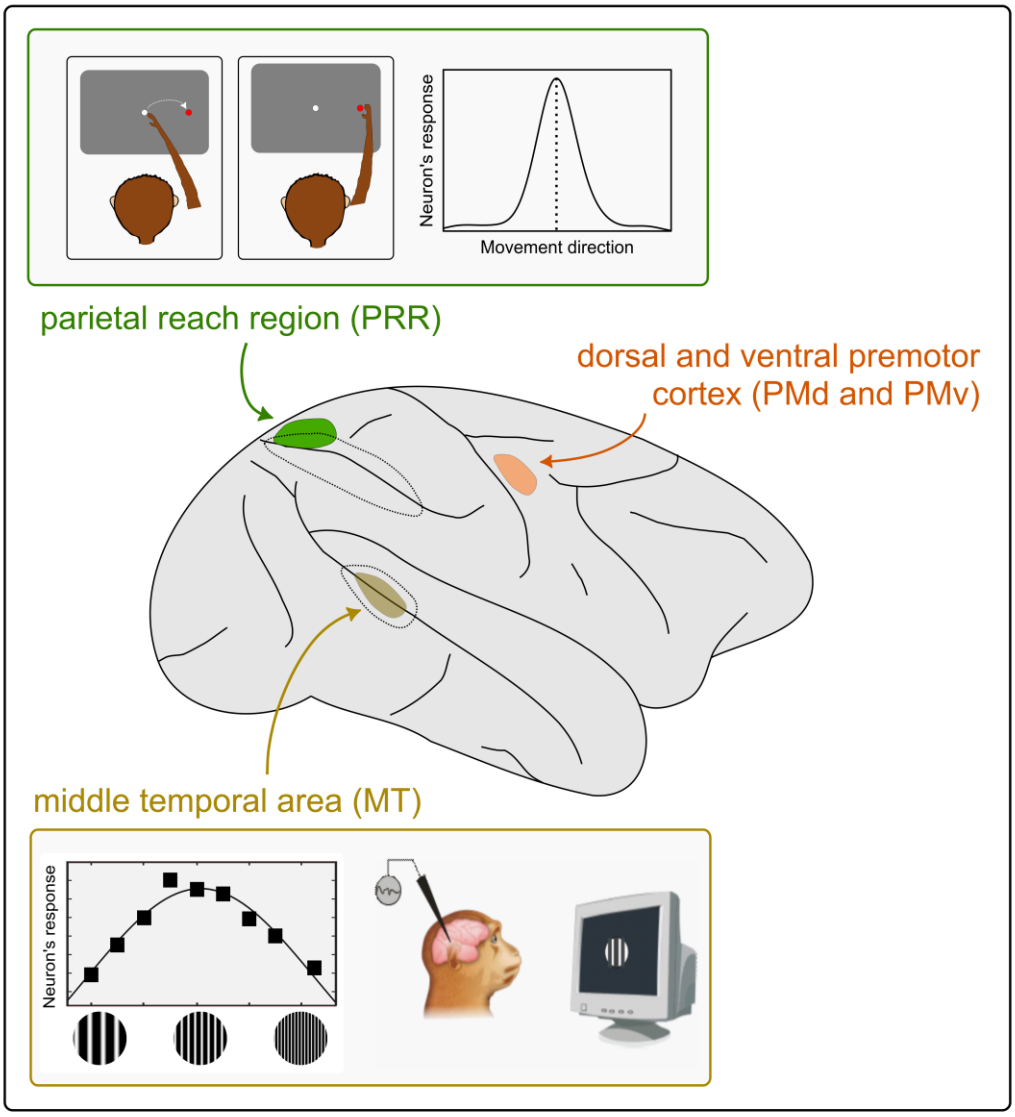

Fig. 1. Neuronal selectivity in monkey brain cortex

A sketch of the monkey brain, in which three colours mark visual (MT), action planning (PRR), and premotor (PM) cortical areas. (The same three colours are used in Figs. 2 and 5 to represent three populations of cortical neurons for comparison with the artificial neuron.) These cortical areas are responsible for different functions: visual perception in area MT (yellow), planning of movement in area PRR (green), and preparation of movement in area PM (orange). Neuronal selectivity in areas MT and PRR is illustrated in the insets. In both cases, the response of a single neuron (measured in the cortex of an alert animal) depends on the relations between properties of the neuron and properties of the stimulus (in sensory neurons) or the planned action (in pre-motor and motor neurons). Thus, in the bottom inset, the neuron is most excited when the animal views a luminance grating presented in the neuron's receptive field at an intermediate spatial frequency, and it is less responsive to high and low spatial frequencies. In the top inset, the neuron is most excited when the animal plans movement in a certain direction within the neuron's response field.

745

746

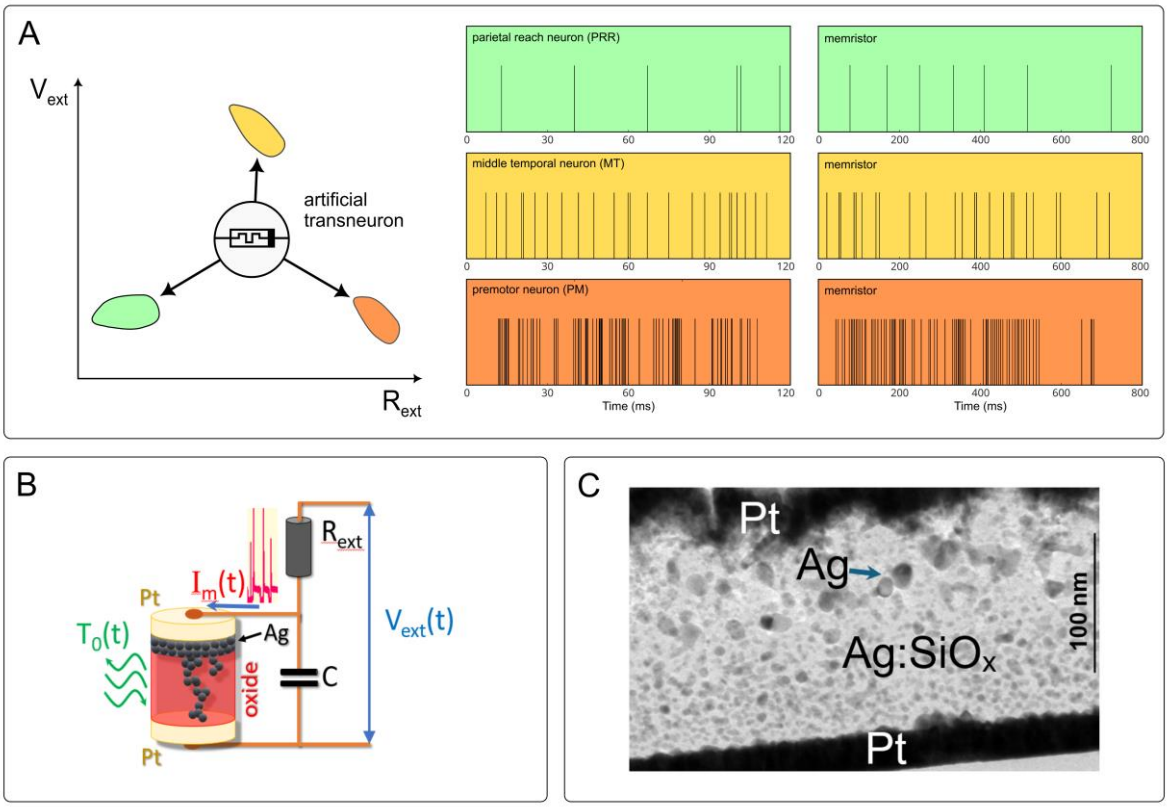

Fig. 2. Artificial transneuron

(A) A conceptual representation of the transneuron moving in the parameter space defined by external voltage V_{ext} and load resistance R_{ext}, reaching distinct regimes of stochasticity. In these regimes, the transneuron emulates the spiking behaviour of biological neurons in the cortical areas shown in Fig. 1, with matching colours. The three pairs of measured spike trains at right illustrate distinct neural response patterns: irregular spiking in area MT, more regular in area PRR, and bursting in area PM. In each pair of plots of the same color, the left plot represent the measured activity of a biological neuron, while the right plot represents the measured activity of the artificial transneuron in a distinct activity regime.

(B) A sketch of the artificial transneuron, with the diffusive memristor represented by the cylindrical element at left. Ag clusters (black dots) diffuse between two Pt electrodes in an SiO_x matrix (reddish medium), forming a filament that connects the memristor terminals. When the memristor, with an internal or external capacitance *C*, is connected in series with an external resistance R_{ext} and loaded by the external voltage V_{ext}, the system generates electric current spikes, I_m (schematically shown in red as $I_m(t)$). The system can be dynamically controlled over time (*t*) by varying the external voltage V_{ext} and the bath temperature T_0 of the SiO_x matrix. This elementary circuit is referred to as an "artificial transneuron" to reflect its ability to emulate the behaviour of biological neurons in different brain areas.

(C) Cross-section TEM image of a diffusive memristor. Two platinum electrodes (Pt) can be seen as capacitor plates with the intervening SiO_x matrix having droplet-like Ag clusters in it. Additional resistance can be either attached to Pt electrodes or realised by depositing a resistive material directly on the Pt electrodes.

747

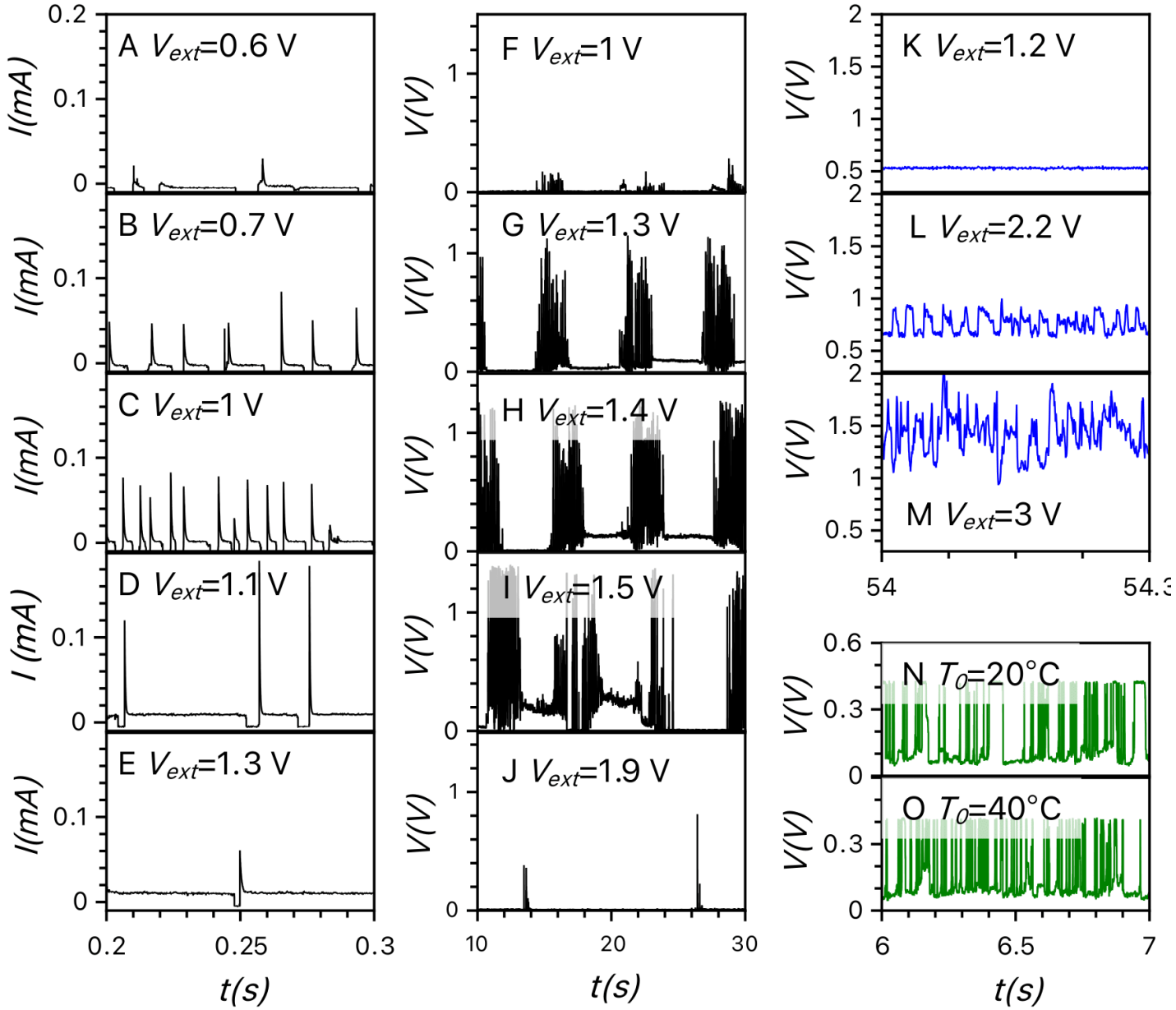

Fig 3. Measured spiking activities of transneurons in different regimes under varying external voltage and temperature. *Left column (A-E):* Measured response of the transneuron in a PRR-like regime; the plots present measurements of current versus time at applied voltages from 0.6V to 1.3V. Within this voltage interval, we observe evolution of regular isolated spikes. Spiking appears at the voltages above 0.6V, grows more intensive for 0.7V and 1V, then decreases for 1.1V and stops for 1.3V. (In these measurements, the external resistance was 68kOhm and the capacitance was 10nF. The memristor was fabricated using Method 1; see Methods.) *Middle column (F-J):* Bursting behaviour of voltage spikes is shown at intermediate voltages (1V-1.9 V). Bursting appears at the voltage of about 1V, develops with the increasing voltage (1.3V and 1.4V), followed by depletion of spiking at 1.5V, and disappears at about 1.9V. (In this transneuron, the external resistance was R_{ext}=65Kohm and the external capacitance was C=50 nF. The sample was fabricated using Method 2.) *Right column (top three panels, K-M):* MT-like spiking of a transneuron (R_{ext}=65Kohm and C=50 nF, fabricated using Method 2). Here, spiking starts at a relatively high voltage threshold of about 2.2V. Then spiking frequency grows as external voltage increases to 2.2V and 3V. The bottom two panels (N-O) at right show the influence of temperature on spiking (for temperatures from 20C to 40C), resulting in a further rise of spiking intensity in this transneuron (with R_{ext}=60 kOhm, C=20 nF, fabricated by Method 2).

748

749

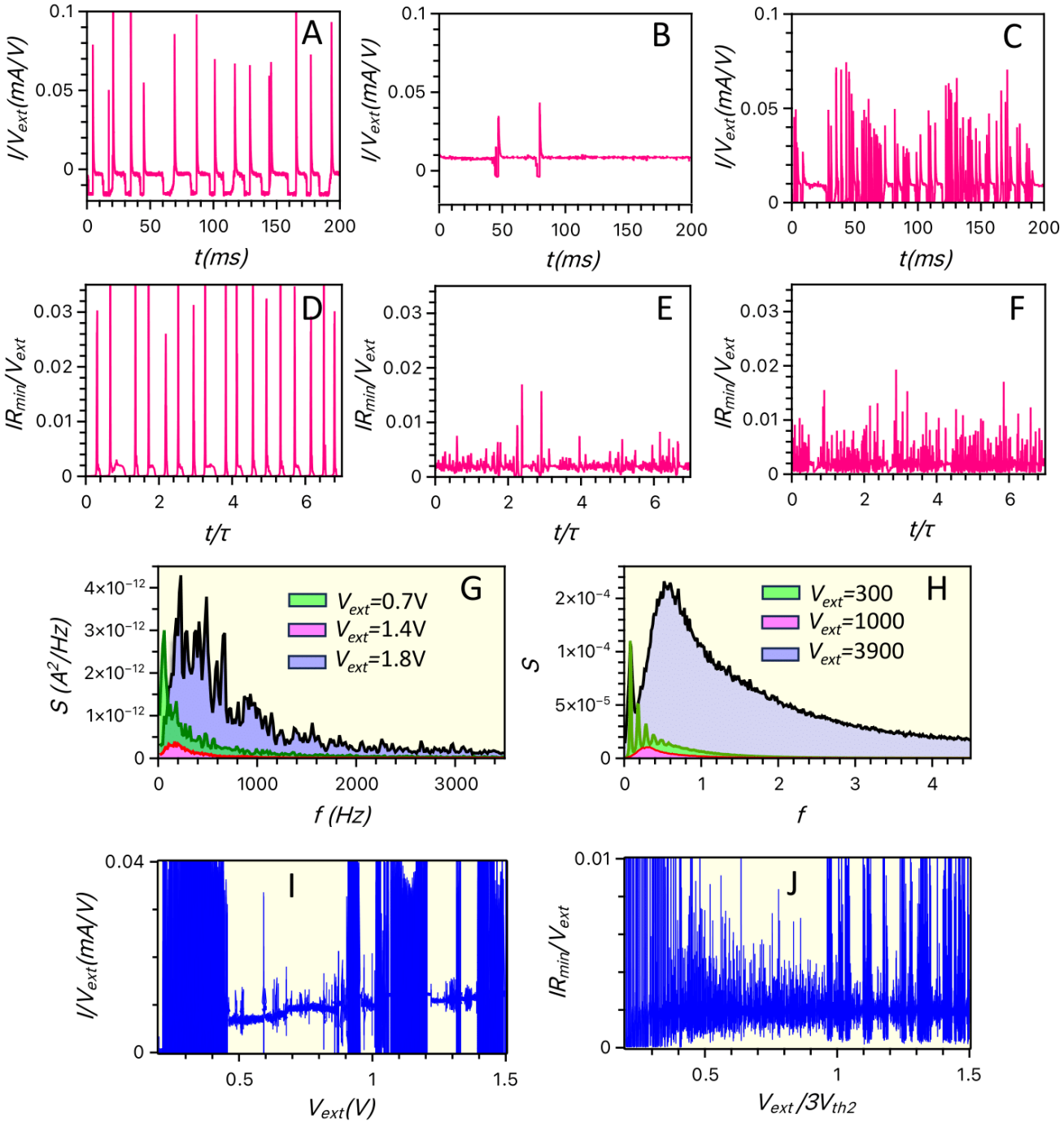

Fig. 4. Three spiking modes of the artificial diffusive neuron. Experimentally measured spiking (A-C) of electrical current in response to the DC voltage applied to the artificial neuron, simulated (D-F) using stochastic Eqs. (1a)-(1c). Regular spiking is observed at low voltages in A and D, sparse irregular spiking is observed at intermediate voltages in B and E, and intermittent bursting is observed at higher voltages in C and F. The measured (G) and simulated (H) power spectra of system responses are represented by red, green, and black curves, respectively. The plots reveal a clear spectral peak (green), indicating regular repetitive spiking at low voltages, a broad spectral maximum (black) at higher voltages, and a weak frequency dependence (red) of the spectra at intermediate voltages, consistent with the spiking modes shown in A-F. The measured (I) and simulated (J) stochastic spiking of current in the diffusive memristor changes gradually as the voltage $V_{\mathrm{ext}}(\mathrm{t})$ varies slowly in time t across the device. The bursting activity at high voltages is separated from regular spiking at low voltages by a regime of sparse spiking. These results demonstrate that voltage can be used to tune the activity of artificial transneurons. (Parameters of simulation are displayed in Table ST1 in SI.)

750

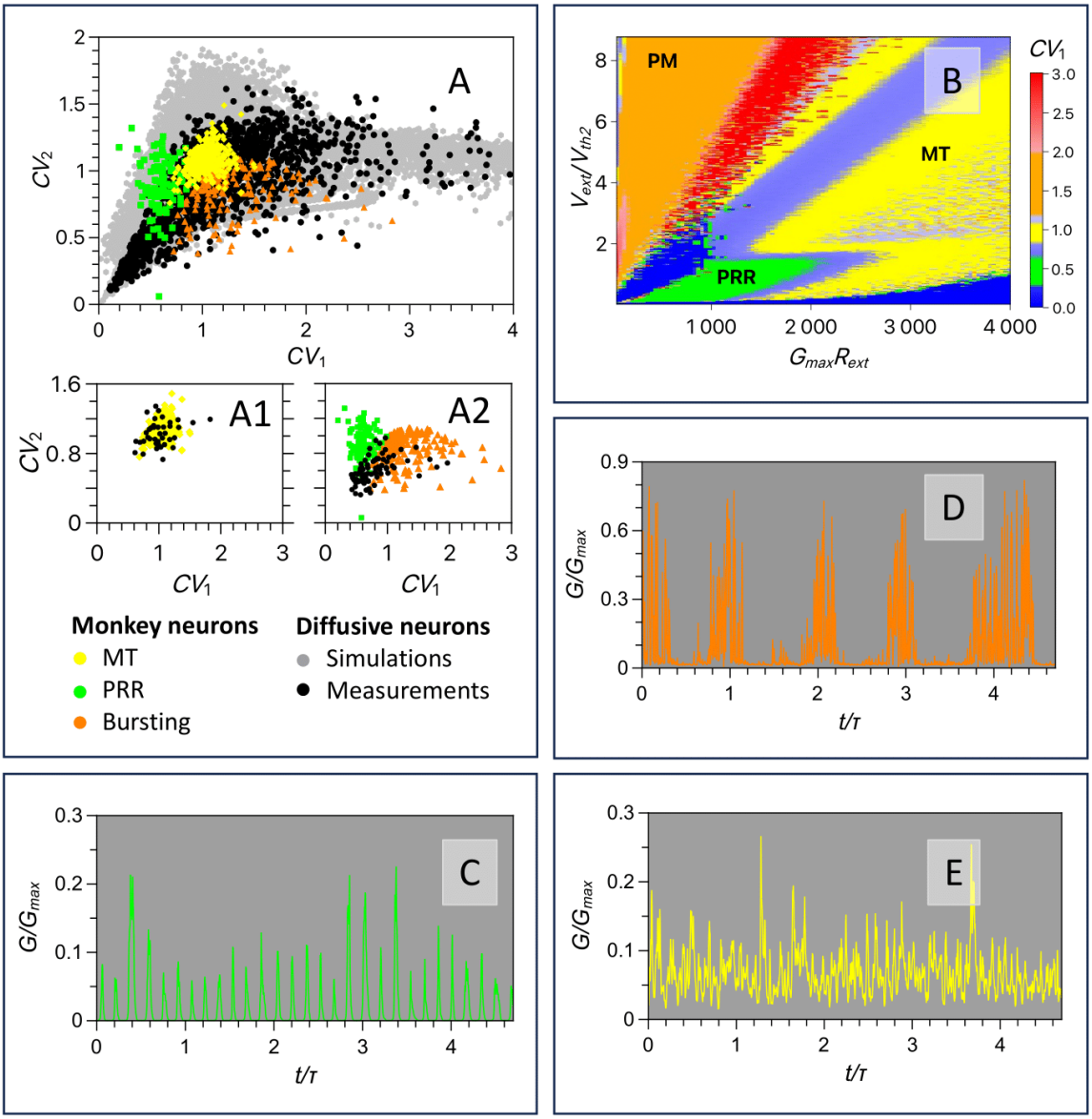

Fig 5. Comparison of biological and artificial neurons. (A) Scatter plots of the coefficients of variation CV_1 and CV_2 obtained (i) by simulating the one Ag-cluster model in Eqs. (1a)-(1c) (grey hexagons), (ii) by measuring of transneurons (black circles), and (iii) by spiking analysis of biological neurons sampled from cortical areas MT (yellow diamonds), PRR (green squares), and PM (orange triangles) in macaque monkeys. Panel A1 shows an overlap between the (CV_1, CV_2) points measured in both MT neurons and the transneuron for R_{ext} = 65 kOhms and C = 1 nF within a voltage interval of 0.6 V to 0.8 V. This plot shows that nearly all transneuron measurements occur within the MT cloud and are well distributed within it. Panel A2 shows that a voltage sweep from 1.06 V to 1.22 V for a transneuron with R_{ext} = 70 kOhms and C = 100 nF shifts the measured (CV_1, CV_2) points of the same transneuron between the PRR and PM clouds. This plot demonstrates the transneuron's ability to transition between the stochastic regimes inherent to biological neurons in different regions of the monkey cortex. (B) The coefficient of variation CV_1 is presented as a color map in a space of external resistance R_{ext} (in units of $1/G_{max}$, with the maximum memristor conductance G_{max}) and external voltage V_{ext} (in units V_{th2} obtained at $G_{max}R_{ext}$=500). The map was obtained by simulations of the artificial neuron [Eq. (1a)-(1c)] with varying load resistance and applied voltage. The regions where the CV_1 of the simulated transneuron corresponds to the CV_1 of biological neurons in cortical areas MT, PRR, and PM are shown respectively in yellow, green, and orange, matching the colours used to label these cortical areas in Figs. 1A and 5A. (C-E) Examples of simulated spiking of transneuron conductance for (CV_1, CV_2) = (0.64. 077), (1.9, 094), and (1.01, 1.05), which correspond to the (CV_1, CV_2) points emulating MT, PRR, and PM neurons respectively, displayed in Fig. 3A. (Simulation parameters are listed in Table ST1.)

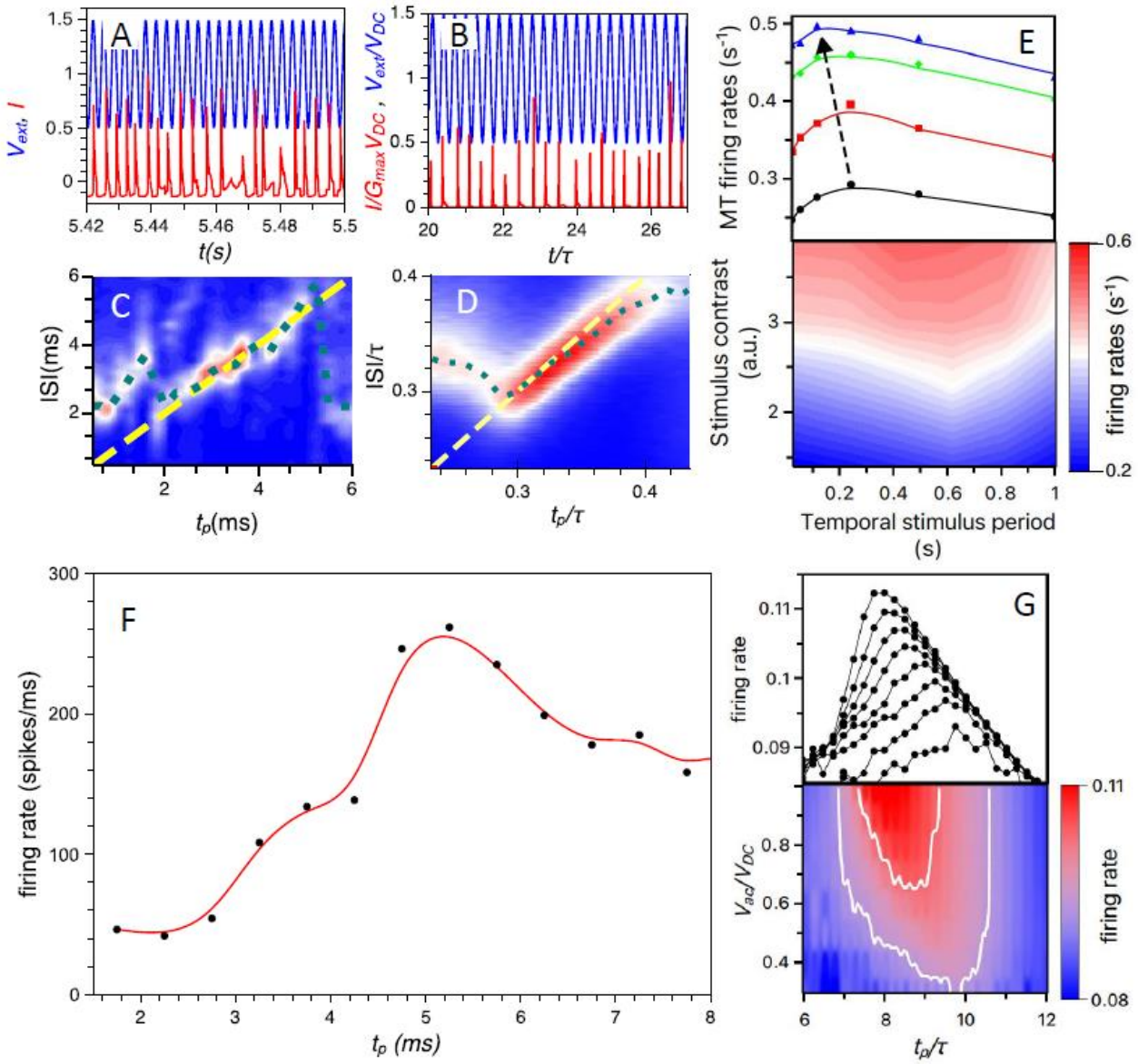

Fig. 6. Selectivity of diffusive neurons. (A) The input voltage signal, $V_{ext} = (1 + 0.5\ \cos 2\pi\ t/t_p)$, is shown in blue for $t_p = 7$ ms, with voltage in volts (V) and time in milliseconds (ms) $[V_{DC} = 1\ V, V_{AC} = 0.5\ V_{DC}, R_{ext} = 70\ kOhm, C = 100\ nF]$. The experimentally measured current response is shown in red, in microamperes (μA). (B) Similar to A, but showing the simulated current response I(t), with V_{DC} equal to the applied voltage (shown in Fig. 2D, corresponding to the self-sustained, no-bursting spiking regime) and for t_p corresponding to the most probable ISI time. Here, the simulated time and ISI are displayed in units of $\tau = R_{ext}C$. (C-D) Contour plots of two-dimensional ISI histograms illustrating neuronal selectivity for the measured (C) and simulated (D) artificial diffusive neurons in the plane of stimulus period t_p (oscillation period) and inter-spike interval (ISI) values. The yellow dashed lines represent the "perfect selectivity conditions" (ISI=t_p) while the dotted green curves show the relationship between the most probable ISI and the stimulus period t_p. Panels C-D can be interpreted as temporal receptive fields of artificial neurons. (E) The measured spiking rate of MT neurons as a function of the stimulus time-oscillation frequency at different luminance contrasts. The maximum rate shifts towards higher frequency (lower oscillation periods) as stimulus contrast increases. (F) The measured spiking rate of the transneuron plotted against the AC-voltage period. The rate exhibits a clear maximum at a specific time (t_p=t^*_p) analogous to the spike rate maximum of MT neurons in panel E. (G) The simulated transneuron spiking rate as a function of the AC-voltage period and amplitude. The bottom panel shows a contour plot, while the upper panel shows individual traces of the functional relationship r(t_p) at different V_{AC}. The period t^*_p, corresponding to the maximum spiking rate, shifts to lower values, consistent with the shift of the maximum spiking rate of MT neurons shown in panel E. (Simulation parameters are provided in Table ST1 in SI.)

753

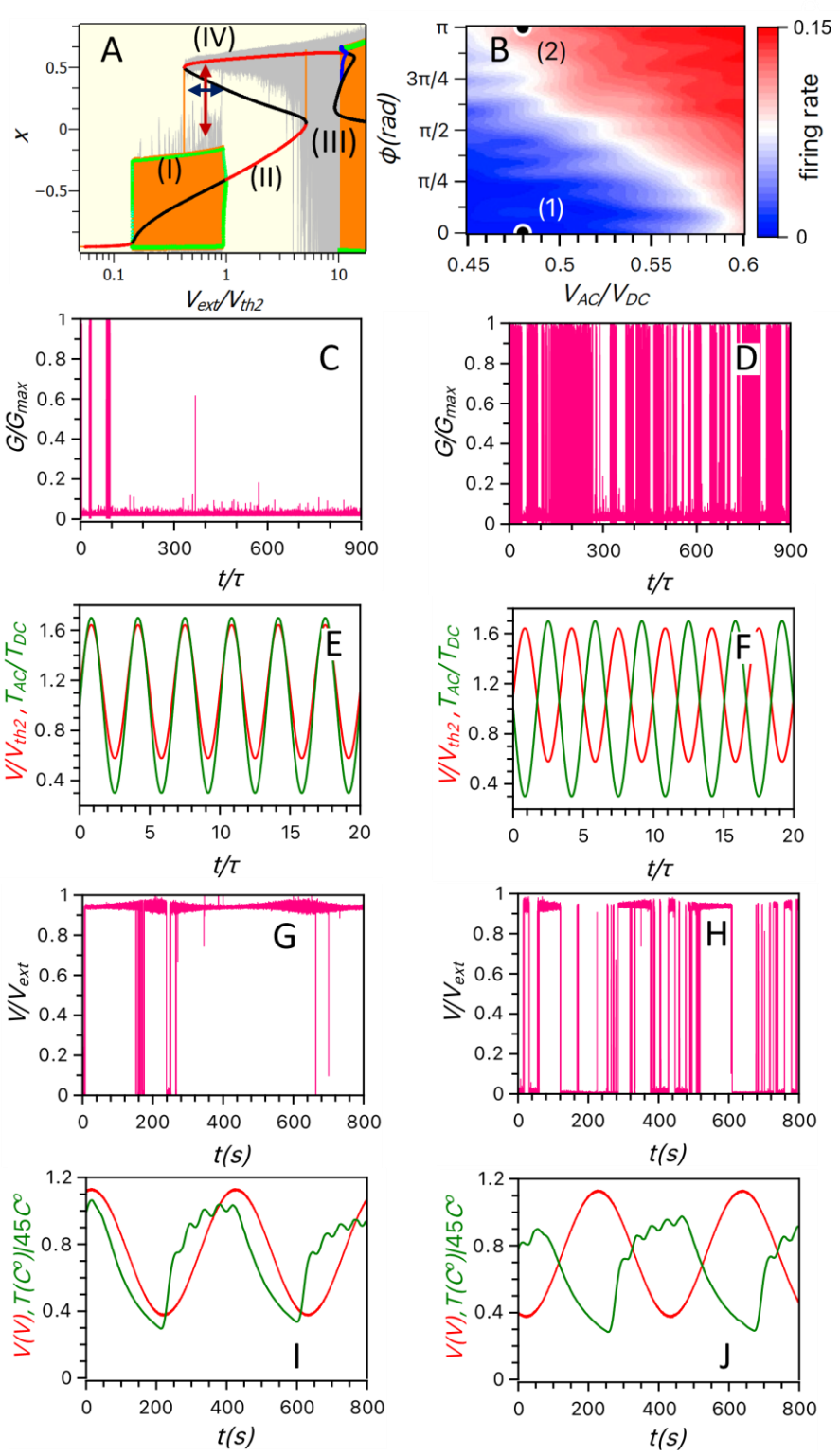

Fig. 7. Signal phase comparator based on transneuron migration between different spiking regimes. **Panel (A)** Phase diagram $(V_{ext}(t), x(t))$ for the one-Ag-cluster model of a diffusive neuron. The diagram is obtained by slowly ramping the external voltage V_{ext} and simulating the cluster trajectory $x(t)$ using stochastic Eq. 1 (light grey curves) and deterministic Eq. 2 (orange curve). Both curves exhibit hysteresis. Two self-sustained spiking modes (labelled I and III) occur at low and high voltages, separated by regions II and IV, which correspond to noise-induced fluctuations producing sparse spiking. From the bifurcation and stability analysis of Eq. 2, we obtained stable (red) and unstable (black) fixed points, where nearby trajectories converge to or diverge from exponentially. This analysis predicts two stable limit cycles, each attracting nearby trajectories to converge corresponding asymptotic oscillations. One cycle is located in Region I and the other in Region III. The oscillatory behaviour of the Ag cluster's position, $x(t)$, alternates between maxima and minima, represented by the green points for each cycle. The bifurcation analysis of Eqs. 2 also predicts an unstable limit cycle (with its maxima and minima shown by blue points), which repels nearby trajectories. For the low voltage spiking mode (regime I), there exists a range of voltages (V_{ext}, indicated by a horizontal blue arrow), where spiking coexists with a stable steady state (Region IV). **Panel (B)** A 2D contour plot of the simulated average spike rates generated by an artificial neuron (Eq. S1) excited by two low-frequency periodic signals. The first signal is the oscillating external voltage $V_{ext} = V_{DC} + V_{AC} \sin \omega t$, and the second is the oscillating bath temperature, $T_0 = T^*(1 + a_T \sin(\omega t + \phi))$. The DC and AC components of these signals are V_{DC} and V_{AC} for the external voltage, and T^* and $T^* a_T$ for the bath temperature. Both signals share the same frequency ω, which is much lower than the average reciprocal ISI. The temperature signal is shifted by phase ϕ. The 2D contour plot demonstrates a strong dependence of the average spike rate on the relative phase ϕ between these two signals. **Panels (C-F):** Two examples of simulated spiking realisations are shown in panels C-D for in-phase (E) and antiphase (F) signals. Minimal spiking is observed for the in-phase signal, while significant spiking occurs for the antiphase signal. Points 1 and 2 in panel (B) correspond to the average spike rates of the realisations shown in C and D. **Panels (G-J):** Measured spiking is shown in G and H for external voltage and temperature, varied in phase (I) and anti-phase (J). Consistent with the simulations illustrated in C-D, the measured spiking is significantly suppressed for in-phase variations (G) compared to the much more intense spiking for anti-phase voltage-temperature oscillations (H). Simulation parameters are provided in Table ST1 in SI.

Supplementary Information (SI) for the manuscript

Artificial transneurons emulate activity in different areas of brain cortex

Rivu Midya, Ambarish S. Pawar, Debi Pattnaik, Eric Mooshagian, Pavel Borisov, Thomas D. Albright, Lawrence H. Snyder, R. Stanley Williams, J. Joshua Yang#, Alexander G. Balanov, Sergei Gepshtein#, Sergey E. Savel'ev#

1. Stochastic and deterministic dynamical equations for transneuron

The physical model of the transneuron is described using stochastic differential equations (see Methods), which have been demonstrated to replicate the findings of numerous prior experiments involving diffusive memristors [27–29, 61]. However, the interplay between stochastic and deterministic forces complicates the differentiation between self-sustained oscillations and noise-induced dynamics.

Here, we qualitatively justify the use of purely deterministic system dynamics to uncover the self-sustained mechanisms underlying spiking behaviour in artificial neurons. To achieve this, we consider a purely deterministic one-cluster model with no external noise, $D_V = 0$. In this case, stochasticity originates from thermal forces acting on the Ag-cluster only. The influence of thermal noise on the cluster's dynamics can be partially replicated by substituting stochastic forces with deterministic thermophoretic and/or thermoelectric forces, as discussed in references [30] and [31] in the main manuscript. Indeed, if we assume that the slowest component of the dynamics is related to the diffusion of the Ag cluster, we can substitute the static solutions of the equations (1b, 1c)

$$T(x) = T_0 + \frac{V^2}{C_{th}\kappa R(x)} = T_0 + \frac{V_{ext}^2 R(x)}{C_{th}\kappa (R(x)+R_{ext})^2} \quad \text{(S1)}$$

to Eq. (1a) and then study the Ag-cluster dynamics in the case of a position-dependent diffusion constant [59]. Therefore, the memristor internal temperature depends on the nanoparticle location, and thermal fluctuations can be replaced by an effective force, which depends on the temperature gradient. The temperature-gradient force plays a key role in the dynamics of the memristor. For example, as was numerically demonstrated in [59], this force produces a dynamical transition in the diffusive memristor: as the voltage increases, a nanocluster trapped in the energy minimum at low voltages jumps to the location with a minimum temperature, which can be attributed to forces arising from entropy gradients. To estimate this force, we assume that both V and T experience deviations from their mean trajectories $V_m(x(t)+\delta x)$ and $T(x(t)+\delta x)$ due to thermal noise. Introducing the spatial derivatives (gradients) of the memristor voltage $V' = [\frac{\partial V(x(t)+\delta x)}{\partial \delta x}]_{\delta x=0}$ and temperature $T' = [\frac{\partial T(x(t)+\delta x)}{\partial \delta x}]_{\delta x=0}$, we derive four coupled deterministic dynamical equations presented in the main manuscript (Eqs. 2a-d). The dimensional version of Eqs. 2a-d used in our simulations is derived in Section 2 of SI.

2. Normalisation of equations

To minimise the number of parameters and simplify model equations (1a-1c) and (2a-2d), we use the following normalisations:

$$t = \tau\frac{\tilde{t}}{30}, x = L\frac{\tilde{x}}{2}, R = R_0\,\tilde{r}(x_1, \dots), R_{ext} = R_0\tilde{R}_{ext}, \quad \text{(S2a)}$$

$$T = \left(\frac{15\eta L^2}{2\tau k_B}\right)\tilde{T}, V = \left(\frac{19\eta L^2}{2q\tau}\right)\tilde{V},\ T_0 = \left(\frac{15\eta L^2}{2\tau k_B}\right)\tilde{T}_0, \quad \text{(S2b)}$$

$$D_V/2 = T_V = \left(\frac{3\eta^2 L^4}{\tau q^2}\right)\tilde{T}_V, U = \left(\frac{15\eta L^2}{2\tau}\right)\tilde{U}, \quad \text{(S2c)}$$

$\lambda = L\tilde{\lambda}/2,\ \tilde{\kappa} = \frac{\kappa\tau}{30}.$ (S2d)

We set $\tilde{\lambda} = 0.12$ and the potential shown in Fig. S1A (the exact profile of the potential $\tilde{U}(\tilde{x})$ is provided in the shared data). In equations (1b) and (2b), $C_{th} = \frac{2.22\eta L^2 k_B}{q^2 R_0}$ resulting in $\tilde{c}_T = 0.18$ in Eq. (S3b) for all our simulations, except for the simulations in Figs. S2B and C, where we use $C_{th} = \frac{20\eta L^2 k_B}{q^2 R_0}$, resulting in $\tilde{c}_T = 0.02$. The integration step for the Euler–Maruyama method is 10^{-5}. Other parameters are given in the table below: for each figure in the main text and supplementary materials. With this normalisation, Eqs. (1a-c) reduce to:

$$\frac{d\tilde{x}_i}{d\tilde{t}} = -\frac{\partial\tilde{U}(\tilde{x}_i)}{\partial\tilde{x}_i} + 0.63(3)\tilde{V} + \sqrt{2\tilde{T}}\,\xi_i(\tilde{t}), \quad \text{(S3a)}$$

$$\frac{d\tilde{T}}{d\tilde{t}} = \tilde{c}_T \frac{\tilde{V}^2}{\tilde{r}(x_1,\ldots x_N)} - \tilde{\kappa}\left(\tilde{T} - \tilde{T}_0\right), \quad \text{(S3b)}$$

$$30\frac{d\tilde{V}}{d\tilde{t}} = \tilde{V}_{ext} - \left(1 + \frac{\tilde{R}_{ext}}{\tilde{r}(\tilde{x}_1,\ldots\tilde{x}_N)}\right)\tilde{V} + \sqrt{2\tilde{T}_V}\varsigma_V(\tilde{t}) \quad \text{(S3c)}$$

With

$$\tilde{r} = \cosh(\tilde{x}_1/0.12)$$

for one particle, and

$$\tilde{r}(\tilde{x}_1,\tilde{x}_2) = (e^{\tilde{x}_1/0.12} + e^{-\tilde{x}_2/0.12} + e^{(\tilde{x}_2-\tilde{x}_1-1)/0.12})/2$$

for two particles in the bottleneck (gap). For Fig. S1E, the charges of two particles were different, reflected by the different coefficients 0.57 and 0.95 for particles *i*=1 and *i*=2, instead of 0.63(3) in Eq. S3a. Comparison Fig. 4J and Fig. S1E reveals that variations in particle charges can further suppress spiking in the noise-induced regime. All the simulations begin with the particles attached to the pillar close to the potential minima $\tilde{x}_1 = -1 + 0.0001, \tilde{x}_2 = -1 + 0.0002, \tilde{T} = \tilde{T}_0, \tilde{V} = 0$.

By normalizing Eqs. (2a)-(2d), we obtain the following dimensionless ordinary-differential equations:

$$\frac{d\tilde{x}}{d\tilde{t}} = -\frac{\partial\tilde{U}}{\partial\tilde{x}} - 0.63(3)\tilde{V} - \tilde{q}_T\tilde{T}' \quad \text{(S4a)}$$

$$\frac{d\tilde{T}'}{d\tilde{t}} = \tilde{c}_T \frac{2\tilde{V}\tilde{V}'\tilde{r} - \tilde{V}^2\tilde{r}'}{\tilde{r}^2} - \tilde{\kappa}\tilde{T}' \quad \text{(S4b)}$$

$$30\frac{d\tilde{V}}{d\tilde{t}} = \tilde{V}_{ext} - \left(1 + \frac{\tilde{R}_{ext}}{\tilde{r}(\tilde{x})}\right)\tilde{V}, \quad \text{(S4c)}$$

$$30\frac{d\tilde{V}'}{d\tilde{t}} = -\left(1 + \frac{\tilde{R}_{ext}}{\tilde{r}(\tilde{x})}\right)\tilde{V}' + \frac{\tilde{R}_{ext}\tilde{r}'(\tilde{x})}{[\tilde{r}(\tilde{x})]^2}\tilde{V}. \quad \text{(S4d)}$$

Here we use an additional normalisation: $T' = (15\eta L/\tau k_B)\tilde{T}',\ q_T = k_B\tilde{q}_T, V' = (19\eta L/q\tau)\tilde{V}'$, and the spatial derivative of dimensionless resistance $\tilde{r}$ was set to $\tilde{r}' = \sinh(\tilde{x}_1/0.12)/0.12$. Initial conditions were the same as in stochastic simulations and $\tilde{T}' = 0, \tilde{V}' = 0$ at $t = 0$.

Table ST1. Parameters of simulations for different figures; the colour of the values matches colour of the graph in the figure.

Table ST1	Fig.4 D/E/F	Fig.4 1G/H	Fig.4 2J	Fig.5A,B	Fig.5 C/D/E	Fig. 6BDH	Fig 7A	Fig. 7B/C/D	Fig. S1F	Fig. S1G
Clusters number	1	1	2	1	1	1	1	1	2	2
$\tilde{\kappa}$	0.9	0.9	0.9	0.9	0.9	0.9	0.9	0.9	0.9	0.9
$\tilde{R}_{ext}$	500	500	500	Varies: 50-5000	2500/50 /3200	500	500	500	1000	1000
$\tilde{T}_0$	0	0	0	0	0	0	0	0.003	0; 0.002	0.002; 0
$\tilde{T}_V$	0	0	0	0	0	0	0	0	0; 0.002	0; 0.002
$\tilde{V}$, $\tilde{V}_{th}=18$	10/30 /195	As in Fig1 DEF	varies: 3.6-81	varies 0-158	24/106 /37	$\tilde{V}_{DC}$=10	0-250	$\tilde{V}_{DC}$ =20 $0.45<\frac{\tilde{V}_{AC}}{\tilde{V}_{DC}}<0.6$ (B) $\frac{\tilde{V}_{AC}}{\tilde{V}_{DC}}$ for C/D in E/F	varies 0-158	varies 0-158

Table ST1	Fig S1C, D($\tilde{q}_T=1$)	Fig S1E $\tilde{q}_1=1.5\tilde{q}$ $\tilde{q}_2=0.9\tilde{q}$	Fig.S2 B/C	Fig. S4	Fig. S7	Fig. S8B
Clusters number	1	2	1	1	1	1
$\tilde{\kappa}$	0.9	0.9	0.1	0.9	0.9	0.9
$\tilde{R}_{ext}$	500	500	500	500	500	500
$\tilde{T}_0$	0	0	0.04/0.4	0, 0.007, 0.02, 0.04, 0.1, 0.2	0	0
$\tilde{T}_V$	0	0	0	0	0	0
$\tilde{V}$, $\tilde{V}_{th}=18$	10/30 /195	varies: 0.2-2.15	158	10	$\tilde{V}_{DC}=195$; $0.3<\tilde{V}_{AC}/\tilde{V}_{DC}<1$	10 ($\tilde{V}_{AC}/\tilde{V}_{DC}$=0.1 and 0.3) 20 ($\tilde{V}_{AC}/\tilde{V}_{DC}$=0.5 and 0.7)

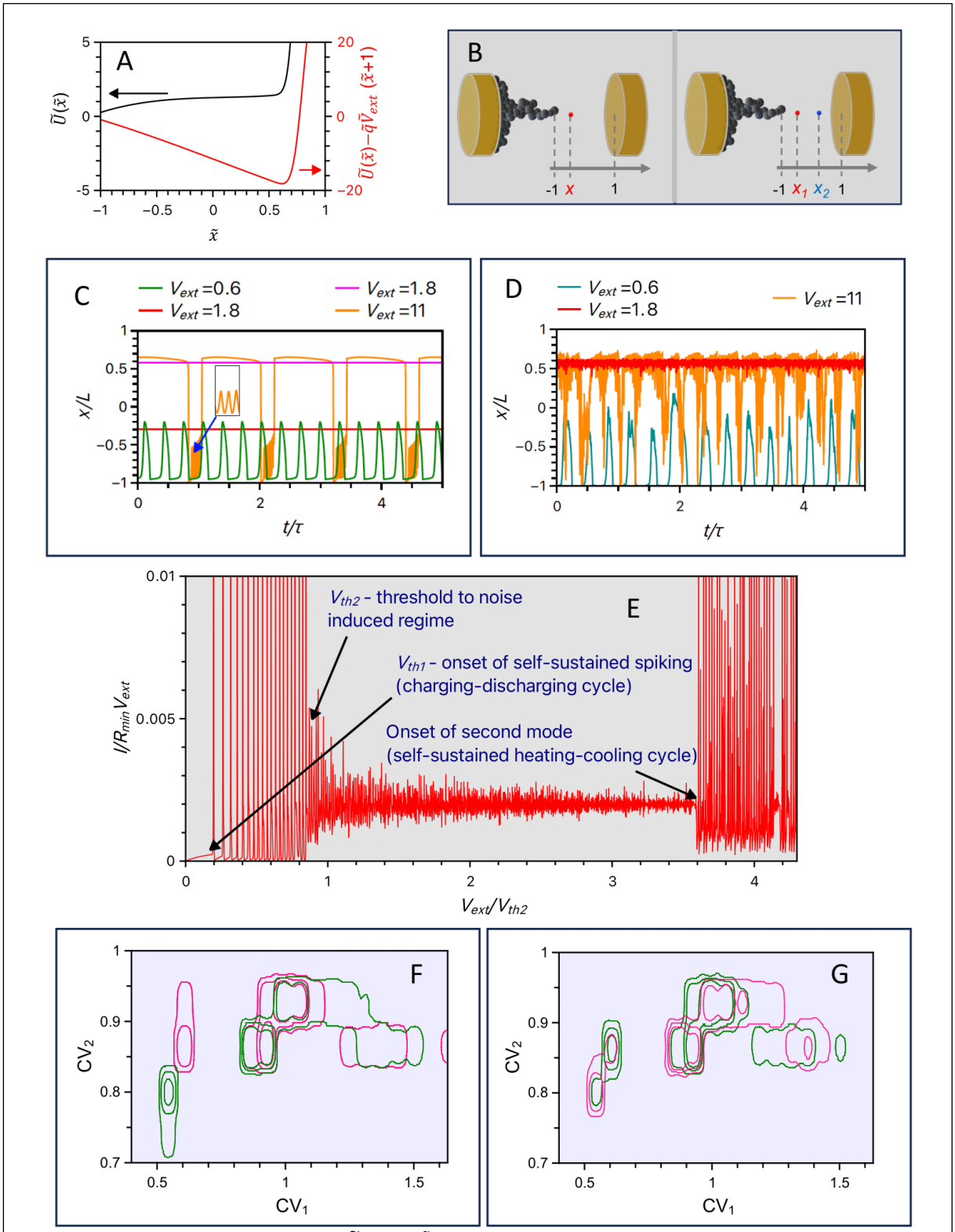

Fig. S1. (A) A voltage-biased potential energy $\tilde{U} - 0.63\tilde{x}\tilde{V}$ used to simulate stochastic dynamics of nanoparticles diffusing in the simulated memristor at zero voltage bias (black curve) and at high external voltages (red curve, $\tilde{V} = 4$). Without voltage bias, the particles are attracted by the tip of the filament (at $\tilde{x}$=-1), while at high voltages the particle diffuses to the minimum (at x=0.6), which is closer to the memristor terminal at $\tilde{x}$=1. This simple potential profile allows to reproduce all experimentally observed dynamical states of the artificial neuron with a diffusive memristor. (B left) A sketch of an Ag particle (red) at position $\tilde{x}$ drifting between the tip of the filament (dark circles) at $\tilde{x}$=-1 and the memristor terminal. (B right) is the same as (B left), but drawn for the case of two particles (one in red one in blue) diffusing in the gap. The yellow cylinders for both (B left) and (B right) represent Pt memristor terminals, one at the base of the filament and the other at $\tilde{x}$=1. Particle trajectory simulations obtained using deterministic (2a-d) and stochastic (1a-c) equations are illustrated in (C) and (D), respectively. Green, red/magenta, and orange curves correspond to, respectively, the regions I, II (with two fixed points), and III of Fig. 7A in the main manuscript. (E) The simulated spiking for slow varying voltage similar to Fig.4J, but for two particles with slightly different induced charges (see details of simulations discussed just after the set of Eqs. S3); (F, G) The distribution of (CV_1, CV_2) points is shown for a transneuron with different types and levels of noise (table ST1, colours of curves match font colours in the table).

3. Self-sustained oscillations of artificial diffusive neurons

To identify the range of voltages where the artificial neuron exhibits self-sustained oscillations, we perform additional simulations using the one-particle dimensional stochastic model (1a-c) [normalised as Eqs. (S3a)-(S3c)] and the deterministic model (2a-d) [normalised as Eqs. (S4a)-(S4d)]. For all the numerical simulations, we use a phenomenological potential $\widetilde{U}\ (\tilde{x})$ (black line in Fig. S1A; the data of the potential profile are shared in the data repository). This potential has one minimum at the tip of the nearly completed conducting filament (i.e., at $\tilde{x}$=-1), which represents attraction of Ag-particles to the filament (sketched in Fig. S1B). Indeed, when the particle is attached to the tip of the filament, the total surface area separating silver and SiO_2 is smaller than in the case when the particle is detached. This means that the surface energy proportional to this surface area has a minimum when the particle touches the pillar tip (Ref. [28] in the main manuscript). When a strong-enough voltage is applied, the total potential $\widetilde{U} - 0.63\tilde{x}\tilde{V}$ is tilted (red line in Fig. S1A), pushing the particle away from the tip of the filament.

The spiking activity illustrated in Fig. S1C-D corresponds to the values of the applied constant voltages chosen in the regions I, II and III of the dynamical phase diagram displayed in Fig. 7A. For the voltage region I, the green curve in Fig. S1C represents the self-sustained oscillations obtained in the deterministic model, while the corresponding stochastic simulations (shown by the green curve in Fig. S1D) exhibit quite regular spiking slightly perturbed by noise. This ''charging-discharging'' cycle originates from the periodically charging capacitor, which causes the voltage drop across the memristor in its high-resistive state to exceed the threshold (the charging part of the cycle). As a result, the memristor switches to its low resistive state followed by a spike of current and a fast voltage decrease (the discharging part of the cycle) destroying the conductive filament and setting memristor to its high resistive state. Then the cycle repeats, starting from the charging part. A close biological analogue of this manner of spiking is the integrate-and-fire mechanism.

For the voltage region II, no spiking is observed in deterministic simulations, as the nanoparticle is attracted to the fixed points at either $\tilde{x} \approx 0.6$ (magenta curve) or $\tilde{x} \approx -0.35$ (red), depending on the initial conditions. Stochastic simulations show fluctuations of the nanoparticle near $\tilde{x} \approx 0.6$ (red curve) due to its larger basin of attraction, as compared to the point $\tilde{x} \approx -0.35$. Physiological studies demonstrate that only the stimulus within the neuron's receptive field can elicit spiking above the level of spontaneous activity. In this regard, the infrequent spiking in the noise-induced spiking mode can be interpreted as the spiking activity observed when the stimulus falls outside of the transneuron's receptive field.

At higher voltages (in region III), the self-sustained oscillations of the nanoparticle between positive ($\tilde{x} > 0.6$) and negative ($\tilde{x} \approx -1$) locations, with a relatively large period, were obtained by simulating the deterministic model (Eqs. S4a-d; the orange curve in Fig. S1C). When the particle is at $\tilde{x} > 0.6$, the system slowly heats up, similar to how resources accumulate in biological neurons before intensive bursting. As soon as the memristor is hot enough, the particle is pushed by thermal fluctuations to a low resistive state, the capacitor discharges rapidly, and the Ag-clusters move toward the edge of the bottleneck ($\tilde{x} \approx -1$). Then, intensive spiking begins. When the nanoparticle is in the region between $\tilde{x}$=-1 and 0, it executes a series of higher-frequency oscillations with a growing amplitude (inset in Fig. S1C) before it returns to the position $\tilde{x} \approx 0.6$, and a new heating cycle begins. These oscillations yield spike trains or bursting spiking behaviour. All of these features were also found in our stochastic simulations (e.g., see the orange curve in Fig. S1D) indicating that we still observe self-sustained oscillations in the presence of noise. In artificial neurons, heating-cooling cycles result in a modulation of the diffusion constant of Ag-clusters due to temperature variations (because, in our formalism, diffusion constant is proportional to Ag-cluster temperature). Although such high-temperature modulations are not observed in biological systems, variations in diffusion constants can significantly influence the dynamics of biological neurons, drawing an analogy to the heating-cooling cycles of spiking observed in artificial neurons [Amir et al., Oscillatory mechanism in primary sensory neurones,

Brain 125, 421 (2002), and Siegelbaum & Tsien, Modulation of gated ion channels as a mode of transmitter action, Trends in Neurosciences 6, 307 (1983)]. In biological neurons, variations in diffusivity may arise, for instance, due to changes in channel shape influenced by fluctuations in ATP or oxygen concentrations in the neuronal environment. These concentrations are, in turn, affected by the spiking activity of the neurons. Specifically, ATP and oxygen levels decrease as they are consumed during neuronal activity, leading to a subsequent slowdown in spiking. Once spiking activity diminishes, ATP and oxygen levels recover, allowing the cycle to repeat.

4. Internal (diffusive) and external (network) noises and their influence on system dynamics

Detailed comparison of how external and internal noises influence the pseudo-deterministic system dynamics requires a separate study of a more complicated neuromorphic circuits with multiple transneurons. Here, we only consider how these noises influence the stochastic characteristics of activity: CV_1 and CV_2. Figures S1F-G present contour-plots illustrating local maxima in the distribution of (CV_1, CV_2). The figures indicate that additional noise sources (either arising from voltage fluctuations or attributed to additional bath temperature T_0) mostly affect the quite regular spiking with CV_1 and CV_2, whose values are comparable to those of PRR biological neurons.

First, we simulated transneuron spiking with $T_0 = D_V = 0$ and $R_{ext}/R_0 = 1000$ for different applied voltages V_{ext}. The corresponding distribution of (CV_1, CV_2) values is shown in Fig. S1F by the olive contour-plot. The two distinctive maxima in the (CV_1, CV_2) distributions correspond to the more regular PRR-like spiking [for (CV_1, CV_2) around (0.55,0.6)] and the less regular (more stochastic) MT-like and PM-like spiking (for CV_1 spanning from 0.9 to 1.5).

Next, a transneuron spiking with (CV_1, CV_2) presented in Fig. S1F with the magenta contour-plot was simulated with both additional internal and external noises originated from the thermal bath and neural network (Table ST1). The cloud of (CV_1, CV_2) points in the distribution corresponding to MT-like spiking is slightly shifted away (and now is detached) from the points corresponding to PM-like spiking, even as both regimes still occupy adjacent areas in the (CV_1, CV_2) space. The cloud of (CV_1, CV_2) points in the distribution that corresponds to PRR-like spiking shifts more noticeably to higher values of CV_1 and CV_2. However, shifting the cloud corresponding to PRR-like simulated activity away from the (CV_1, CV_2) area that corresponds to biological PRR neurons requires a much stronger noise than used in the simulation. This observation highlights the robustness of all the (CV_1, CV_2) transneuron clouds associated with the stochastic behaviours of biological neurons in PRR, MT, and PM.

We have also compared the specific influence of the internal thermal bath alone, and of the external voltage noises alone, on the distribution of (CV_1, CV_2) points for transneuron spiking (Fig. S1G, olive and magenta curves, respectively). The simulations show that adding either of these noise sources alone affects the shape of the (CV_1, CV_2) distribution in a way similar to the case where both sources are present (compare Fig. S1F and Fig. S1G). Namely, the PRR-like cloud of (CV_1, CV_2) points shifts to higher values CV_1 and CV_2, and the MT-like and PRR-like clouds of (CV_1, CV_2) are divided into several islands. This is evidence that main findings of this study are robust to different types of noise and different noise intensities.

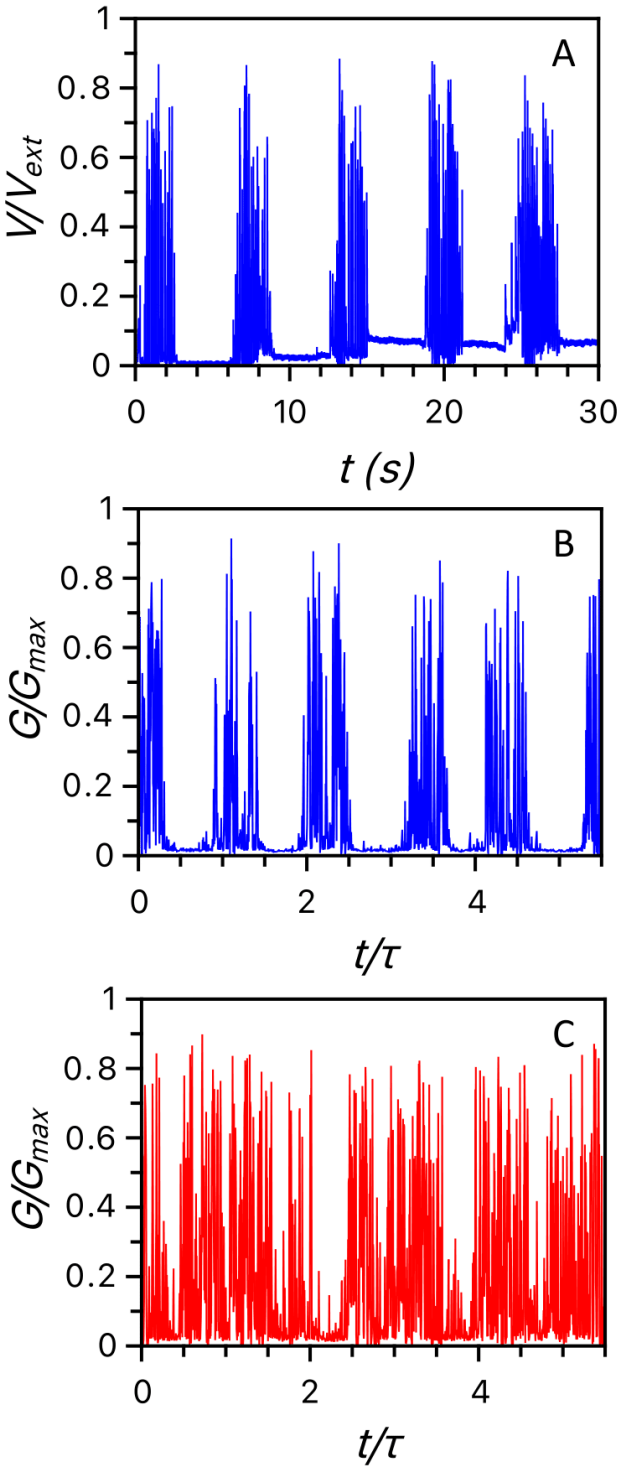

Fig. S2 (A) Experimentally measured bursting activity, which is voltage across the memristor normalised by the applied voltage. (B) Simulated bursting for the same parameters as in Fig. S1D (orange curve) but with κ and $\tilde{c}_T$ being nine times lower than in Fig. S1D. (C) The same as panel B yet at higher temperatures (see table ST1). Blue and red traces represent, respectively, the situations with low and high noise in the system.

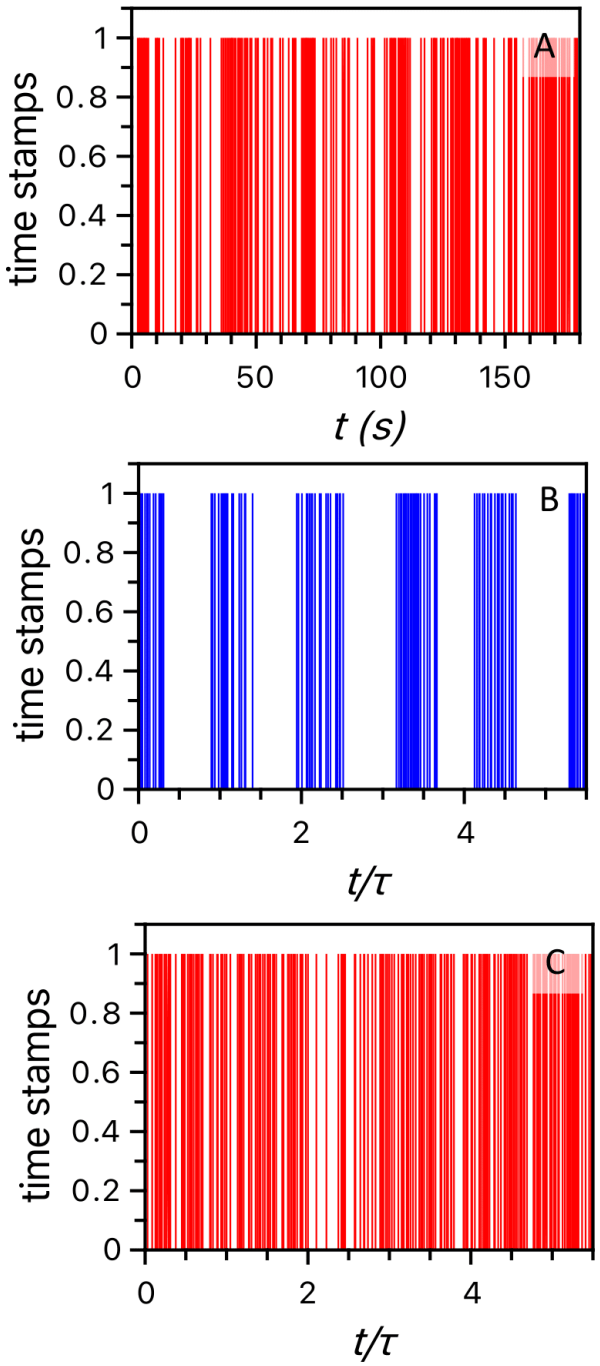

Fig. S3 (A) Timestamps of spikes in a bursting biological neuron (sampled from the data shown in Fig. 5 of the main text). (B-C) Timestamp of spikes obtained using the threshold of G/G_{max}=0.1, corresponding to the simulated data in Figs. S2B and S2C, respectively.

979

5. Bursting of transneurons and biological neurons: measurements and simulations.

Depending on the range of voltage V_{ext}, the cooling constant κ, and the load resistance R_{ext}, the observed and simulated activity at higher voltages has the form of either the partly overlapping spiking trains (as in Fig. 4C, F) or separate bursts of spiking (Fig. S2A-B). The lower the value of the cooling constant κ, the longer is the time interval between the successive spiking trains. These separated bursts are expected when the duration of heating needed to raise the temperature of Ag-clusters is much longer than the mean inter-spike interval. In this case, the memristor will stay in the intermediate resistive state for a long time (i.e., in the state where the cluster is stuck near the point of $\tilde{x} \approx 0.6$) with no spiking, resulting in the quiet intervals between bursts. The temperature will slowly rise, reaching the energy of the barrier that separates spiking and non-spiking dynamics. As soon as the temperature is high enough, thermal fluctuations push the memristor to its high resistive state in which the Ag-cluster is attached to the tip of the filament. In this state, the Ag-cluster starts to move repetitively between the tip and the middle of the gap, switching the memristor between the high and low resistive states, producing charging-discharging oscillations of the memristor's capacitor, and generating current spiking within a single train. In agreement with this analysis, the well separated spiking trains (Fig. S2B) have been observed in our simulation when the value of κ is lower than that in Fig. 4C. The experimentally observed bursting portrayed in Fig. S2A demonstrates similar spiking trains with long quiet intervals between them. (The evolution of bursting with the applied voltage is shown in Fig. 3.)

We also represent spiking by means of timestamps (Fig. S3B-C), with the spikes registered when the simulated signal, G(t), exceeds the threshold of $G/G_{max}=0.1$ and $G_{max}=1/R_0$. According to our simulations, an increase of the bath temperature T_0 results in noisier bursting (Fig. S2C), which corresponds to the less regular spiking bursts in the timestamp picture (Fig. S3C). In the latter figure, the vertical lines of equal height are shown at the instants of spike occurrence. The simulated noisy bursting (Fig. S3C) has common features with the bursting of premotor neurons illustrated in Fig. S3A. This suggests that tuning the bath temperature by additional heating or cooling the chipset with memristive device allows diffusive transneurons to emulate spiking of biological neurons at different levels of stochasticity.

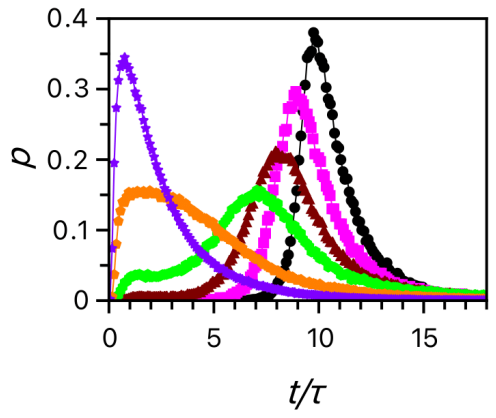

Fig. S4 Simulated evolution of the distributions of ISIs in an artificial neuron for parameters corresponding to Fig. S1D (green curve) with the temperature of the bath T_0 increasing (see table ST1 in which font colours correspond to the data point colours used in this figure). At low temperatures (black, magenta, and brown symbols) ISI probability densities have a clear peak corresponding to a self-sustained spiking mode (as in Fig. 4A, D). The distributions are well approximated by Gamma distributions. At higher temperatures (orange and violet symbols), the distribution evolves towards a Poisson-like distribution with the most probable value of ISI approaching zero.

6. Control of stochasticity by bath temperature of artificial diffusive neurons

As seen in the previous section (Section 5 of SI) of Supplementary Information, bath temperature significantly affects the noisy pattern of bursting (Fig. S2, S3) in the cooling-heating self-oscillating regime of the system (regime III in Fig. 7A and orange curves in Fig. S1C-D). Here we demonstrate how temperature affects ISI distribution for the first oscillating mode (PRR-like quite regular spiking) related to charging-discharging the capacitor in the regime I in Fig. 7A (illustrated by the spiking pattern in Fig. 4A, D and by the green curve in Fig. S1D).

Most simulations presented in the main text were performed for the background temperature much lower than the temperature change due to Joule heating (i.e., we neglected T_0). The reason is that the voltage drop occurs across a very small gap between

the filament and the terminal (see Fig. S1B), resulting in a high local temperature of the Ag-cluster in the gap, as compared to the bath temperature. Here we consider how increasing the background temperature affects the statistics of inter-spike intervals (Fig. S4). At low temperatures, the ISI distribution has a pronounced maximum far from zero; here the ISI statistics are described well by the Gamma distribution, similar to the commonly observed ISI statistics in biological neurons (Ref. [36] in the main text). With increase of T_0, the noise in the system becomes more intense, which makes the self-sustained spikes more frequent and less regular. Therefore, as T_0 increases, the maximum of the distribution gradually shifts towards low ISI values and the distribution peak broadens. Simultaneously, an additional broad local maximum emerges at near-zero ISI, corresponding to the additional noise-induced spikes triggered by the large-enough fluctuations. For even higher values of T_0, the maximum corresponding to self-sustained oscillations is suppressed completely, and the distribution approaches the Poisson distribution. Thus, varying the background temperature allows for additional tuning of stochasticity in artificial diffusive neurons helping to emulate the desired statistical features of different types of biological neurons.

7. Dependence of stochastic characteristics on stimulus intensity or contrast

Spiking of biological neurons could be triggered ("evoked") by stimulation or it can be spontaneous. In our physiological experiments with visually stimulated MT neurons, the measured spiking is necessarily characterised by both spontaneous and evoked components. For more intensive

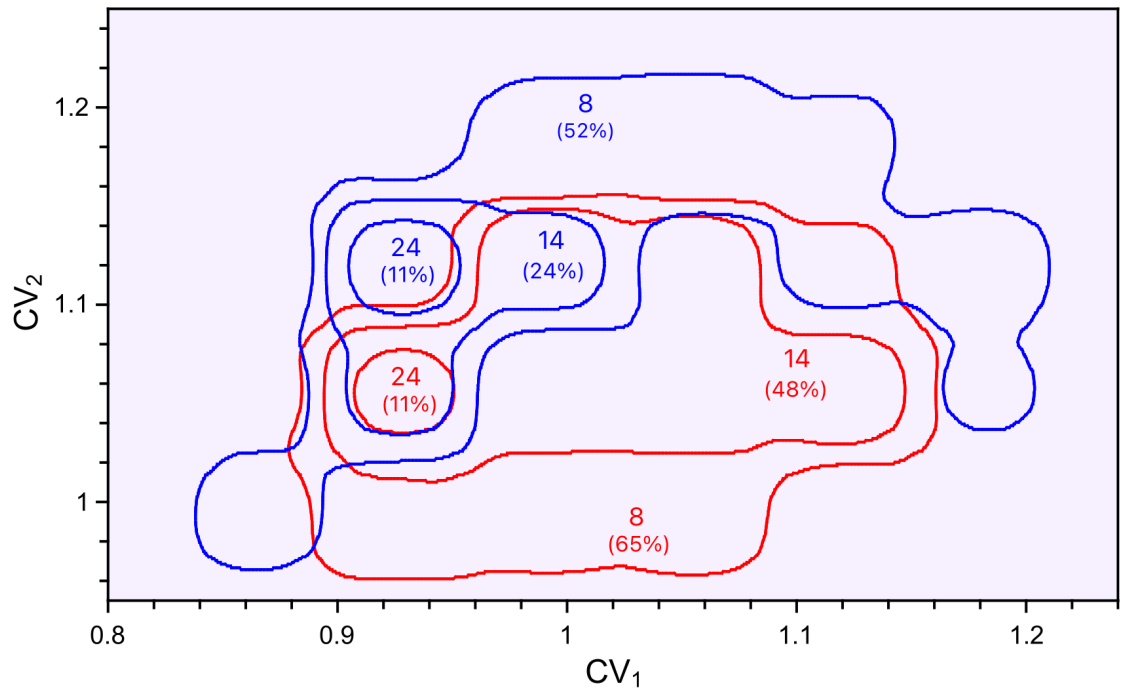

Fig. S5. Contour plots of the distributions $\rho(CV_1, CV_2)$ of (CV_1, CV_2) points for MT biological neurons under two combined contrasts of visual stimulation: the contour plot in blue for contrasts 0.5% and 1.9%, and the contour plot in red for contrasts 26.6% and 100%. The numerical values displayed near each closed contour correspond to the values of the ρ taken at the corresponding contours, while the per-cent values represent the probability that a (CV_1, CV_2) point is found inside the contour.

stimulation, the evoked activity increases, suggesting a method for estimating the relative influence of evoked and spontaneous spiking. Such analysis can be useful for comparing the activities of biological neurons and artificial transneurons. For the latter, the AC-voltage component can be attributed to stimulation, and the DC-voltage component can be seen as a driver of both spontaneous and evoked spiking, depending on the information coding protocols (e.g., Fig. 6 in the main text).

To understand how stimulus intensity influences spiking of biological neurons, we focus on how the activity of MT-neurons depends on visual stimulus contrast. Fig. S5 illustrates the (CV_1, CV_2) distributions for low- and high-contrast stimuli (blue and red contour-plots, respectively). To improve

statistical power of our analysis, we combine (CV_1, CV_2) distributions for two lowest contrasts (0.5% and 1.9%) and two highest contrasts (26.6% and 100%) of visual stimuli. It is evident that the contour-plots for high and low contrasts significantly overlap, and that the maximum of the distribution is shifted to lower values of CV_2 for higher- contrast stimuli, even as the maxima of both distributions are found at nearly the same values of CV_1. This indicates that, in MT neurons, the higher intensity of visual stimulation makes the values of the nearest interspike intervals slightly more similar to one another (increasing the local coherence of spike sequences) while having little effect on the overall ISI distribution. The significant overlap of the distributions demonstrates that the values of (CV_1, CV_2) are controlled mainly by the internal dynamics of different types of neurons, justifying our approach to accumulate all (CV_1, CV_2) values for each cortical area regardless of stimulus intensity.

8. Overlapping estimates of measured stochastic characteristics in transneurons and biological neurons.

By changing DC voltage and/or external resistance, the stochastic characteristic of a transneuron can be tuned to different areas in the (CV_1, CV_2) plane. To understand what fraction of biological neurons in cortical areas MT, PRR, and PM can be mimicked by transneurons, we first identify the convex hull (red shadowed region) of the measured points (shown in Fig. S6A as black circuits) for transneurons at different DC voltages and different external resistances and capacitances. We then count the number of (CV_1, CV_2) points for each type of biological neuron (MT, PRR, or PM) inside this region and divide the result by the total number of (CV_1, CV_2) points for the corresponding type of neuron. The resulting fractions of the overlap of MT, PRR, and PM (CV_1, CV_2) covered by the convex hull of the measured transneuron (CV_1, CV_2) points are 100%, about 70%, and 100% (see Fig. S6).

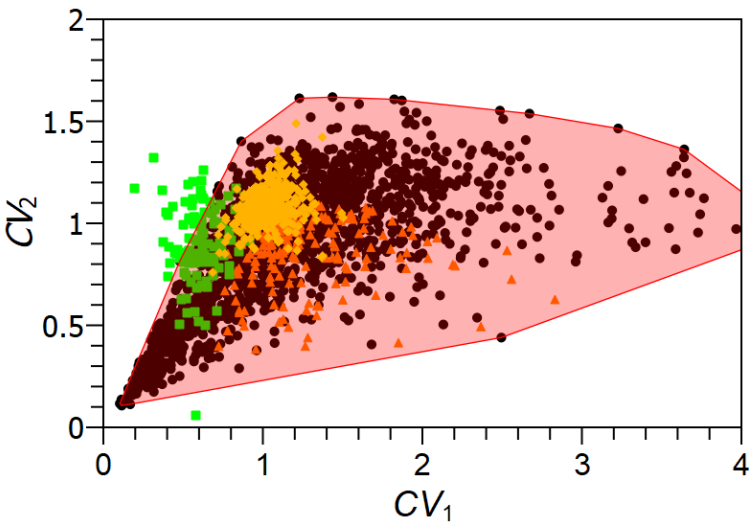

Fig. S6. The overlap of (CV1, CV2) points for the spiking of biological neurons across different cortical areas and transneurons measured at various external voltages, resistances, and capacitances. The red-shadowed convex hull plotted for the measured (CV1, CV2) data set for transneurons, encompasses 100% of the MT (CV1, CV2) points (yellow), approximately 70% of the PRR (CV1, CV2) points (green), and 100% of the PM (CV1, CV2) points (orange).

9. Selectivity of mode 2 spiking (cooling-heating oscillations)

Figs. 6C-D, G in the main text illustrate transneuron's selectivity in the quite regular spiking mode (such as in Fig. 4D). Selectivity manifests itself in a sharpening of the ISI distributions (Fig. 6C-D) when AC-

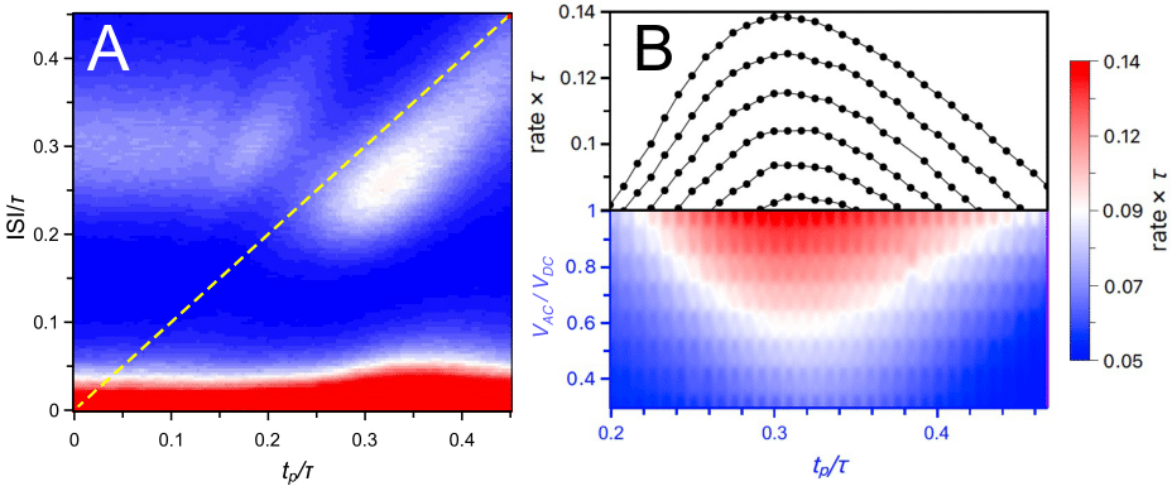

Fig. S7 (A) The simulated distribution of ISI intervals for the same parameters as in Fig. 6 but with the DC voltage corresponding to Fig. 4F. (B) The average spiking rate as a function of AC-period for the same parameters as in (A) and AC amplitude changing from 0.3 V_{DC} to V_{DC}. Simulation parameters are displayed in Table ST1.

voltage is applied with a period approaching to that of the neuron's mean ISI (which, in turn, is close to the natural spiking time [6]). Selectivity also manifests itself as the maximum spiking rate near the natural spiking time (Fig 6G). Such selectivity can be found also in other spiking regimes of the transneuron.

To demonstrate how neuronal selectivity changes with increasing stochasticity, in Fig. S7 we plot ISI distributions and the spiking rate for a more stochastic spiking regime (as in Fig. 4F, corresponding to stochastic noisy bursting). The ISI distribution shows that a large fraction of spiking occurs at short values of ISI (red region in Fig. S7A). Nevertheless, a less pronounced maximum of the distribution (as compared to Fig. 6D) is observed at larger values of ISI (white region) and is characterised by the intrinsic time scale. However, when the AC-period (represented by the yellow dashed line) reaches the intrinsic ISI time, the white cloud becomes more pronounces and it is "dragged" by stimulation along the yellow line. These features are similar to the case of selectivity reported in the main text (Fig. 6D). Moreover, when the AC-period is close to the natural (or most probable) ISI, the spiking at low values of ISI becomes more intense (indicated in Fig. S7A by the red "bump" in the distribution, at low values of ISI, at t_p of about 0.35τ). These effects cause the spiking rate to have a maximum (Fig. S7B), in close analogy to the behaviour of selectivity observed in Fig. 6G in the main text. Finally, with increasing stimulus intensity (the amplitude of AC voltage), we observe a shift of the period at which the spiking rate reaches its maximum, toward a lower value of the period (i.e., a higher AC-frequency). This observation is consistent with the nonlinear ''resonance'' drift of the maximum of spiking reported in the main text for the case of quite regular spiking (Fig. 6G) and for biological MT neurons (Fig. 6E).

10. "Beyond rate" information coding

Here, we focus on (a) how the self-sustained and noise-induced spiking regimes can be used for encoding and processing information "beyond spike rate" coding and (b) how stimulus contrast can influence spiking of transneurons. The common rate coding hypothesis holds that information about sensory stimuli is encoded in the firing rates of cortical neurons, while other statistical properties of

ISI sequences are not essential. This view of neural function competes with other information coding paradigms, such as temporal coding [Gerstner, W., Kistler, W. Spiking neuron models: single neurons, populations, plasticity. *Cambridge University Press* (2002)], in which spiking statistics other than rate play an important role.

In the present study of biological and artificial neurons, we observed that ISI statistics inconsistent with the simple notion of scaling of ISI distributions with the firing rate (Fig. S8A-C). Such a scaling assumes that the shape of the ISI distribution does not change significantly as stimulation increases [Reich, D., Victor, J., Knight, B. The power ratio and the interval map: Spiking models and extracellular recordings. *J. Neurosci.* **18**, 10090 (1998)]. However, if these distributions are significantly affected by stimulation, then ISI statistics can be used for encoding and processing of information in biological and artificial neurons. Our physiological measurements show that an increase of stimulus strength (e.g., an increase of stimulus luminance contrast) can significantly affect the shape of ISI probability distributions (Fig. S8A). As stimulus contrast increases, ISI distributions for most MT neurons become narrower with more pronounced peaks (as in Fig. S8A, right panel), implying a change of response toward a more regular spiking activity. Still, some neurons counterintuitively exhibit a shift toward a more stochastic behaviour, resulting in a lowering and broadening of ISI distributions (Fig. S8A, left panel).

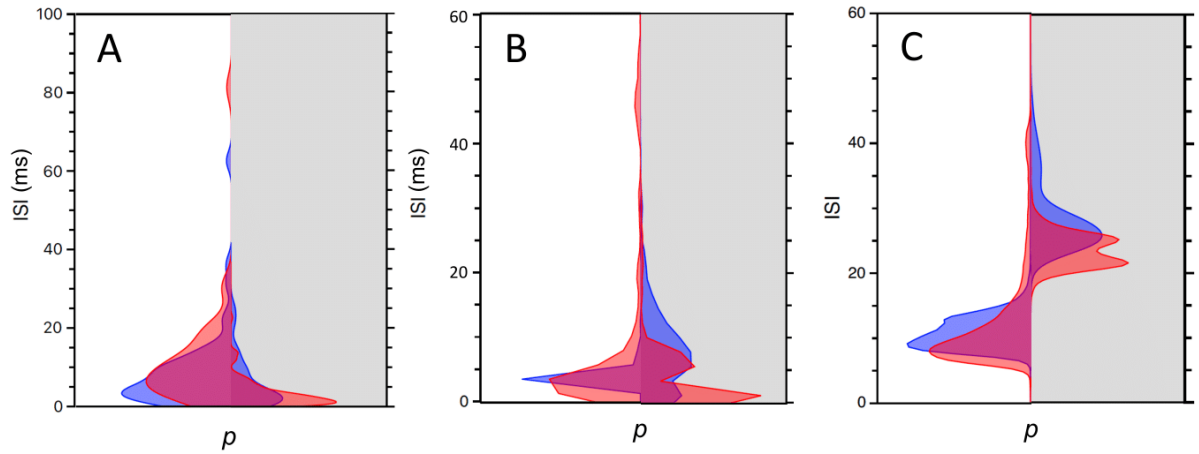

Fig. S8: Violin plots for high AC-amplitudes and contrasts are shown in red, and for low AC-amplitudes and contrasts are shown in blue, for two biological middle temporal (MT) neurons (A) that responded differently to an increase of stimulus strength, for the measured artificial neuron (B), and for the simulated transneuron (C). The DC voltages for measured and simulated artificial neurons were selected from the noise-induced spiking mode (as in Fig. 4B, E) and from the self-sustained spiking mode (as in Fig. 4A, D) shown, respectively, in the right and left panels of each violin plot.

Remarkably, we observe similar behaviour in our experiments with the artificial diffusive neuron driven by DC and AC voltage: $V_{ext} = V_{DC} + V_{AC} \cos \omega t$. To better understand the transformation of ISI distributions in artificial transneurons, we consider the cases where the transneurons are tuned to the boundary between noise-induced (Fig. 4B, E) and self-sustained (Fig. 4A, D) spiking regimes. If a transneuron is in the noise-induced mode at $V_{AC} = 0$, the arrival of a stimulus, $V_{AC} > 0$, can occasionally drive the neuron into the regime of self-sustained oscillation. Stronger stimuli (e.g., at higher AC voltage amplitude) increase the contribution of self-sustained oscillations in the neuron's activity, leading to a more regular spiking (see right panels of Fig. S8B for measurements, and Fig. S8C for simulation). However, if the neuron already dwells in the regime of self-sustained spiking at $V_{AC} = 0$, then increasing stimulus intensity eventually drives the neuron into the noise-induced regime, reducing regularity of spiking (see left panels of Fig. S8B for measurements, and Fig. S8C for simulation).

This method of controlling the ISI distribution transcends rate scaling, and it relies on the ability of the transneuron to change its spiking mode while excited by stimulation.

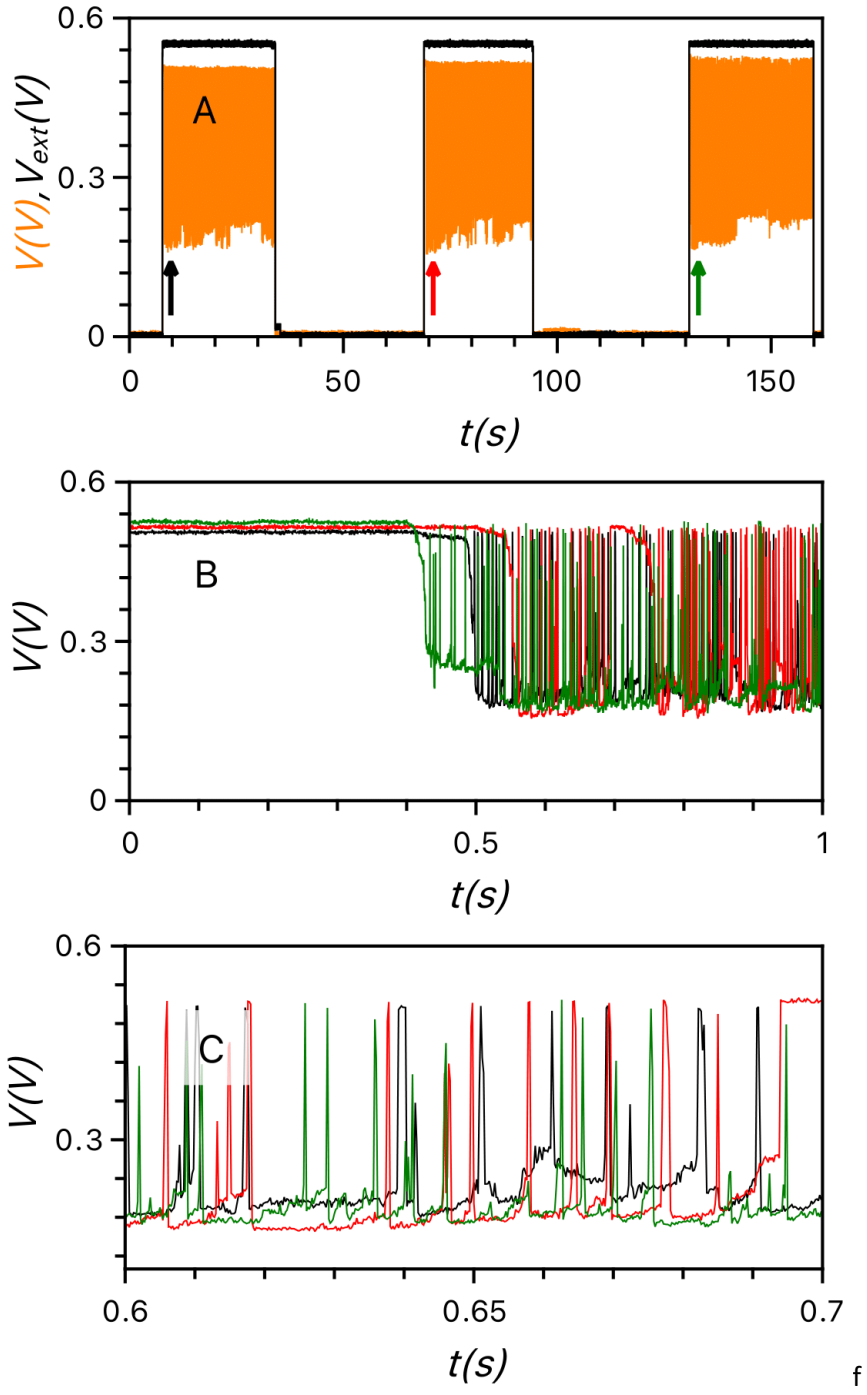

Fig. S 9. (a) Three pulses of external voltage (black line) of 30 sec separated by 35 sec of idle (zero applied external voltage) intervals and the corresponding spiking of voltage across the memristor (magenta line) for the transneuron with R_{ext}=65k Ohm and C= 50nF. Arrows indicate parts of spiking sequence enlarged in (b-c) with the colours of arrows corresponding to the colours of spiking curves in the panels below. This repetitive measurement shows that the transneuron's response is truly stochastic, with random delays of spiking after the beginning of each pulse (the time count in b-c starts from the moment of application of the corresponding voltage pulse) and irregular spiking for all three pulses with the not-coinciding peaks.

11. Repetitive measurements of transneuron spiking

In Fig. S9 we demonstrate a truly stochastic nature of spiking in transneurons. Namely, we measure system response to three voltage pulses separated by idle periods (when no external voltage is applied), which allow the system to relax and reset. Despite the same voltage applied in each pulse,

the spiking response to each pulse is characterized by different delays [28] relative to the pulse onset. The spiking patterns triggered by the pulses do not reproduce themselves even though they are characterized by similar stochastic features.

12. Small functional neuromorphic circuits with transneurons

Simple neuromorphic circuits capable to perform multi-signal comparison can be fabricated using modern thin-film equipment instead of wiring connections between artificial neurons (Fig. S10). This approach may resolve the problem of scalability of neuromorphic devices.

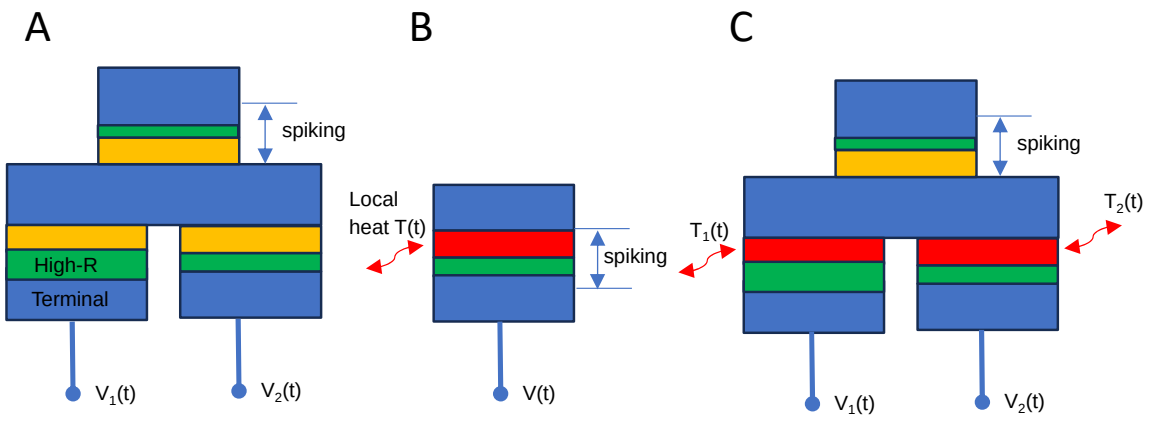

Fig. S10: (A) Three spiking artificial neuron block, which can be fabricated as a unit, rather than three separate neurons wired in a neuromorphic circuit. Blue layers correspond to memristors' terminals (e.g., Pt layers), green layers correspond to high-resistive materials used as external resistances, while yellow layers represent memristive layers. This block can be used for comparing two signals encoded in time-dependent voltages V_1 and V_2. This system can be used, for example, to compute the direction of sound or to evaluate the distance to an object. (B) One transneuron block with the red layer marking Ag-SiO diffusive memristor. This transneuron can perform two-signal comparison as in (A) encoded now in voltage and temperature signals as described in the main text. (C) Circuit arrangement for signal comparison performed by two transneurons with one artificial neuron used as readout. The signals (e.g., two for visual information and two for sound information) in $T_1(t)$, $T_2(t)$, $V_1(t)$, $V_2(t)$, can be used, e.g., for directional and distance estimation, thus identifying the location of an object.

Comparing the proposed transneurons with less tuneable artificial neurons based on volatile memristors (such as NbO devices), one can conclude that similar neuromorphic transneuron circuits could perform significantly more complex computations. Indeed, as shown above, one transneuron can perform two-signal comparison (Fig. 10SB), which requires a network of three artificial neurons (Fig. 10A). Such neuromorphic circuits can be used to estimate the distance from, or the direction to, the source of a signal, e.g., visual *or* auditory. A network of three transneurons (Fig. S10C) can potentially handle multimodal signals (e.g., visual *and* auditory), and thus greatly expand the capabilities of neuromorphic hardware.

The fabrication procedure for such devices could include the following steps. One could start with a clean and polished semiconducting substrate, such as a 500 µm GaAs wafer. On the polished and epitaxial side of the wafer, a gold sink layer (~200nm) could be deposited using sputtering or e-beam evaporation, to ensure smoothness and uniformity. Next, photolithography and liftoff could be performed to create two windows. The memristor layer can then be sputter deposited (e.g., Ag:SiOx, of approximately 50 nm), followed by deposition of a high resistive layer (e.g., Nichrome, of approximately 20nm), and then by deposition of a top gold contact layer (approximately 100 nm). After stripping the unexposed photoresist, two memristor mesa structures should be revealed on the polished side of the substrate with gold top electrodes for electrical connections. The substrate could then be bonded to a glass disk with the memristor side attached to the glass using wax. The backside of the substrate would then be thinned by lapping and polishing to a minimum thickness of approximately 50 µm. The next step would be to remove the entire GaAs substrate. A controlled etching of the GaAs substrate (e.g., bubble etch) can be performed until the gold layer becomes visible,

stopped once the entire gold sink layer is exposed. Further photolithography and deposition processes can be conducted to fabricate the third memristor layer on the backside of the now-etched wafer (on the gold sink layer). Finally, the fabricated device can be demounted from the glass disk, resulting in a flexible gold film with three memristor layers (as depicted in Fig. S10).

13. Details of physiological studies

Recordings in cortical area MT

Animals. Two adult male rhesus monkeys (*Macaca mulatta*) of ages 11 and 12 were used in this study. Experimental protocols were approved by the Salk Institute Animal Care and Use Committee and conform to US Department of Agriculture regulations and to the National Institutes of Health guidelines for the humane care and use of laboratory animals. Procedures for surgery and wound maintenance have been described in detail elsewhere [Dobkins, K.R., Albright, T.D., What happens if it changes colour when it moves?: the nature of chromatic input to macaque visual area MT. *J. Neurosci.* **14**, 4854 (1994) and Refs. [32, 34] in the main manuscript].

Apparatus. All visual stimuli were generated using Matlab (The MathWorks Inc, Natick) software using a high-resolution graphics display controller (Quadro Pro Graphics card, 1024x768 pixels, 8 bits/pixel) operating in a Pentium class computer. Stimuli were displayed on a 21-inch monitor (75 Hz, non-interlaced, 1024x768 pixels; model GDM-2000TC; Sony, Tokyo, Japan). The output of the video monitor was measured with a PR650 photometer (Photo-Research, Chatsworth, CA), and the voltage/luminance relationship was linearized independently for each of the three guns in the cathode ray tube.

Behavioural procedure. Monkeys were seated in a standard primate chair (Crist Instruments, Germantown, MD) with the head post rigidly supported by the chair frame. The task was to fixate a small (0.2 deg diameter) target in the presence of moving visual stimuli for the duration of each trial (500-2000 msec). The target was presented on a video display at a viewing distance of 57 cm in a dark room (<0.5 cd/m^2). The mean background luminance of the monitor was 15 cd/m^2. Eye position was sampled at 120 Hz using an infrared video-based system (IScan, Burlington, MA). The eye position data were monitored and recorded with the CORTEX program (Laboratory of Neuropsychology, National Institute of Mental Health, Bethesda, MD), which was also used to implement the behavioural paradigm and to control stimulus presentation. After eye position was maintained within a 2 deg window centred on the fixation target throughout the trial, animals were given a small (0.15 cc) juice reward.

Electrophysiological procedure. A craniotomy was performed to allow for electrode passage into area MT. Activity of single units was recorded in area MT using tungsten microelectrodes (3-5MΩ; Frederick Haer Company, Bowdoinham, ME), which were driven into cortex using a hydraulic micropositioner (model 650; David Kopf Instruments, Tujunga, CA). Neurophysiological signals were filtered, sorted, and stored using the Plexon (Dallas, TX) system. Visual responses were recorded from 139 directionally selective MT neurons in two awake, fixating macaque monkeys (74 and 65 neurons in Monkeys 1 and 2, respectively). We measured firing rates to stimuli at five to seven different levels of luminance contrast (0.05-100%) at the preferred spatiotemporal frequencies: five spatial frequencies (SF) and one to five temporal frequencies (TF). The different stimulus conditions and contrasts were interleaved in random order across trials.

Data resampling. For each neuron, the firing rates estimated in separate trials within each condition of stimulus frequency and contrast were resampled with replacement. The number of samples was ten (which is the number of trials employed in the experiments). Response functions were fitted to the resampled data using non-parametric polynomial regression, repeated for 500 iterations of resampling to estimate errors of peak SF within each condition. The errors were used to measure

differences between peaks across stimulus contrasts. A similar procedure was used to estimate errors of peak TF for each condition.

Recordings in cortical area PRR

Animals. All procedures conformed to the Guide for the Care and Use of Laboratory Animals and were approved by the Washington University Institutional Animal Care and Use Committee. Two male rhesus macaques (*Macaca mulatta*; Monkey 1 and Monkey 2) participated in the study.

Apparatus. Head-fixed animals sat in a custom-designed monkey chair (Crist Instruments, Hagerstown, MD) with a fully open front to allow unimpaired reaching movements. Visual stimuli were back-projected by an LCD projector onto a translucent Plexiglas screen mounted vertically, 40 cm in front of the animal. Eye position was monitored using the 120-Hz ISCAN eye-tracking laboratory (ETL-400). Touches were monitored every 2 ms using capacitive sensors, mounted at the home pads and behind the Plexiglas projection screen. Touch positions on the screen were organized in a 3x3 grid centred on the fixation point. Plexiglas dividers were mounted on the front of the screen at the middle of each target location. The animals were trained to reach with the left paw to the left side of the divider and with the right paw to the right side of the divider. A capacitive sensor was placed to either side of each target location, such that the left and right paws activated unique sensors even when both paws reached to the same target. Animals were monitored in the testing room at all times using an infrared camera equipped with an infrared illuminator.

Behavioural procedure. The animals performed delayed saccades or reaches with the left, right, or both arms [Mooshagian, E., Wang, C., Ferdoash, A., Snyder, L.H., Movement order and saccade direction affect a common measure of eye-hand coordination in bimanual reaching, *J. Neurophys.* **112**, 730 (2014)]. Animals first fixated on a circular white stimulus (1.5x1.5°) centred on the screen in front of them. Left and right paws touched "home" pads situated at waist height and 20 cm in front of each shoulder. After 500 ms of holding the initial eye (+/-3°) and hand positions, either one or two peripheral target(s) (5x5°) appeared on the screen. When two targets appeared, they were at opposite locations relative to the fixation point, e.g., left/right or up/down (see below). After an additional 1,250 to 1,750 ms, the central eye fixation target shrank in size to a single pixel, cueing the animal to move to the peripheral target(s) in accordance with a code conveyed by target colour. A green target instructed a left forelimb reach, a red target instructed a right forelimb reach, a blue target instructed a combined reach with both arms, and a white target instructed a saccade (no reach). Trials could be unimanual or bimanual. Bimanual trials could have a single target ("bimanual together") or two targets separated by 180° ("bimanual apart"). All trial types were interleaved. On saccade and unimanual reach trials, the unused hand(s) were required to remain on the home button(s) throughout the trial. On reach trials, eye movements were unconstrained once the go cue appeared. On bimanual trials, the left and right paws were required to hit their target(s) within 500 ms of one another. Spatial tolerances were +/-3° for reaches and +/-2° for saccades. When an error occurred (a failure to achieve or maintain fixation or to touch the home buttons throughout the delay period or a movement that did not achieve the required spatial tolerance), the trial was aborted, and a short (1,500 ms) timeout ensued. Aborted trials were excluded from further analyses. Successful trials were rewarded with a drop of water or juice. Data were collected during 67 and 53 sessions in Monkey 1 and Monkey 2, respectively.

Electrophysiological procedure. Recordings were made from both hemispheres of 2 adult male rhesus monkeys. Recording chambers were centred at approximately 11mm posterior to the ear canals and 8mm lateral of the midline and placed flush to the skull. Extracellular recordings were made using glass-coated tungsten electrodes (Alpha Omega; electrode impedance 0.5–3.0 MΩ). Neurophysiological signals were filtered, sorted, and stored using the Plexon (Dallas, TX) system. Neurons were recorded along the caudal portion of the intraparietal sulcus (IPS). PRR does not fit neatly into any single anatomical area, but instead lies at the boundary of MIP and PO/V6A, though it

also extends slightly towards the lateral bank, towards lateral occipital-parietal (LOP) area (Ref. [37] in the main manuscript and in [Mooshagian, E., Wang, C., Holmes, C. D., and Snyder, L. H. Single units in the posterior parietal cortex encode patterns of bimanual coordination. *Cereb. Cortex* **28**, 1549–1567 (2018)]. We therefore functionally define PRR as that region of cortex containing a large proportion of neurons with visual transients and with sustained delay activity that is substantially greater for combined reaches plus saccades compared with saccades alone in most cases. This functional definition covers much of anatomical areas PO and V6a, on the medial bank of the IPS and rostral bank of the parieto-occipital sulcus, the posterior half of the medial intraparietal area (MIP) on the medial bank, and a portion of LOP on the lateral bank. This definition distinguishes PRR from nearby lateral intraparietal area (LIP), which lies on the lateral bank immediately rostral to LOP and where most neurons show similar responses to combined reaches plus saccades compared with saccades alone.

While searching for neurons, animals performed saccade and right arm only (contralateral) trials as described above. Previous work established that few neurons are active for ipsilateral but not contralateral reaches, and even those neurons are somewhat active during saccades [Chang, S.W., Dickinson, A.R., Snyder, L.H., Limb-specific representation for reaching in the posterior parietal cortex. *J. Neurosci.* **28**, 6128 (2008)]. Online, the preferred direction was defined as the target location that resulted in the largest sustained firing during the delay period for the single target reach conditions (contralateral arm, ipsilateral arm, both arms together). The null direction was defined as the target location 180° from the preferred direction relative to the central fixation point. The preferred direction of the neurons with data for all directions was confirmed by offline analysis. We computed the modulation for each condition for each neuron as the activity for a movement in the preferred direction minus activity for a movement in the null direction. A single preferred direction was determined for each neuron and applied to all tasks.